# Mercury oxidation from bromine chemistry in the free troposphere over the Southeastern US

**S. Coburn[1,2], B. Dix[1], E. Edgerton[3], C. D. Holmes[4], D. Kinnison[5], Q. Liang[6], A. ter Schure[7], S. Wang[1,2,#], R. Volkamer[1,2]**

[1] {Department of Chemistry and Biochemistry, University of Colorado Boulder, Boulder, CO, USA}

[2] {Cooperative Institute for Research in Environmental Sciences (CIRES), Boulder, CO, USA}

[3] {Atmospheric Research and Analysis (ARA) Inc., Plano, TX, USA}

[4] {Department of Earth, Ocean and Atmospheric Science, Florida State University, Tallahassee, FL, USA}

[5] {National Center for Atmospheric Research (NCAR), Boulder, CO, USA}

[6] NASA Goddard Space Flight Center, Atmospheric Chemistry and Dynamics Branch, Greenbelt, MD 20771, USA

[7] {Electric Power Research Institute (EPRI), Palo Alto, CA, USA}

[#] {now at: Department of Chemistry, University of Michigan, MI, USA}

**Revised manuscript submitted to Atmospheric Chemistry and Physics on 27 February 2016**

**Abstract**

The elevated deposition of atmospheric mercury over the Southeastern United States is currently not well understood. Here we measure partial columns and vertical profiles of bromine monoxide (BrO) radicals, a key component of mercury oxidation chemistry, to better understand the processes and altitudes at which mercury is being oxidized in the atmosphere. We use the data from a ground-based MAX-DOAS instrument located at a coastal site ~1 km from the Gulf of Mexico in Gulf Breeze, FL, where we had previously detected tropospheric BrO (Coburn et al., 2011). Our profile retrieval assimilates information about stratospheric BrO from the WACCM chemical transport model, and uses only measurements at moderately low solar zenith angles (SZA) to estimate the BrO slant column density contained in the reference spectrum ($SCD_{Ref}$). The approach has 2.6 degrees of freedom, and avoids spectroscopic complications that arise at high SZA; knowledge about $SCD_{Ref}$ helps to maximize sensitivity in the free troposphere (FT). A cloud-free case study day with low aerosol load (9 April 2010) provided optimal conditions for distinguishing marine boundary layer (MBL: 0-1 km) and free tropospheric (FT: 1-15 km) BrO from the ground. The average daytime tropospheric BrO vertical column density (VCD) of ~$2.3 \times 10^{13}$ molec $cm^{-2}$ (SZA<70°) is consistent with our earlier reports on other days. The vertical profile locates essentially all tropospheric BrO above 4 km, and shows no evidence for BrO inside the MBL (detection limit < 0.5 pptv). BrO increases to ~3.5 pptv at 10-15 km altitude, consistent with recent aircraft observations. Our case study day is further consistent with recent aircraft studies, in that the oxidation of gaseous elemental mercury (GEM) by bromine radicals to form gaseous oxidized mercury (GOM) is the dominant pathway for GEM oxidation throughout the troposphere above Gulf Breeze. The column integral oxidation rates range from 3.5-$3.7 \times 10^5$ molec $cm^{-2}$ $s^{-1}$ for bromine, while the contribution from ozone ($O_3$) is $0.8 \times 10^5$ molec $cm^{-2}$ $s^{-1}$. Chlorine induced oxidation is estimated to add <5% to these mercury oxidation rates. The GOM formation rate is sensitive to recently proposed atmospheric scavenging reactions of the HgBr adduct by nitrogen dioxide ($NO_2$), and to a lesser extent also $HO_2$ radicals. Using a 3-D chemical transport model, we find that surface GOM variations are typical also of other days, and are mainly derived from the free troposphere. Bromine chemistry is active in the FT over Gulf Breeze, where it forms water-

soluble GOM that is subsequently available for wet scavenging by thunderstorms or transport to the boundary layer.

## 1 Introduction

Measurements of tropospheric halogen species are an area of increasing research interest due to the ability of halogens to destroy tropospheric ozone ($O_3$) (Read et al., 2008; Saiz-Lopez et al., 2012), oxidize atmospheric mercury (Holmes et al., 2009; Hynes et al., 2009), and modify oxidative capacity (Parella et al., 2012). Most assessments of the impacts of halogen chemistry are based on measurements of halogen oxides (bromine monoxide (BrO) and iodine monoxide (IO)), since these radicals are typically found at higher concentrations throughout the troposphere than the corresponding halogen atom radicals. Many of these studies take place in the planetary boundary layer (PBL) given that this region of the atmosphere is easily accessible from measurements located at the surface, and is also the most directly impacted by anthropogenic activities. However, halogen chemistry in the free troposphere (FT), albeit more challenging to measure, has the potential to affect an even larger air volume and mass. In particular, the colder temperatures of the free troposphere accelerate the bromine oxidation of gaseous elemental mercury (GEM) (Donohoue et al., 2006). Satellite-borne measurements represent a powerful resource for assessing global distributions and tropospheric vertical column densities (VCD) of BrO (GOME – van Roozendael et al., 2002; GOME-2 - Theys et al., 2011; Sihler et al., 2012). However, satellite retrievals rely on assumptions made about the vertical distribution of BrO, and uncertainties in these assumptions can lead to over/under predictions in the derived tropospheric VCD. The most direct method for measuring trace gas vertical distributions is through the use of aircraft (Prados Ramon et al., 2011; Volkamer et al., 2015), or balloons (Fitzenberger et al., 2000; Pundt et al., 2002; Dorf et al., 2006). However, this type of measurement is costly and potentially impractical if the goal is to establish long term trends in the FT. Ground-based measurements are typically more straightforward to deploy and maintain for extended periods of time, but optimizing ground-based capabilities to observe the FT remains an area of active research (Schofield et al., 2006; Theys et al., 2007; Hendrick et al. 2007; Coburn et al., 2011). Specifically, ground-based Multi-Axis Differential Optical Absorption

Spectroscopy (MAX-DOAS) measurements are uniquely suited for this type of study since this technique also assesses vertical distributions, and derived VCDs can be directly compared with models and satellites. Additionally, the DOAS retrieval allows for the detection of not only BrO, but also other trace gases that have significant impacts on the chemical cycling of bromine species in the atmosphere, such as $NO_2$ and some volatile organic compounds (VOCs). However, measurements of FT BrO from ground-based MAX-DOAS are not straightforward for several reasons: 1) stratospheric BrO represents a large portion of the measured signal and creates a background that has to be accounted for when attempting to assess the FT; 2) ozone absorption structures are strongly present in the same wavelength region as BrO and can create interferences due to stratospheric ozone absorption, in particular at high solar zenith angles (SZA) (Aliwell et al., 2002; van Roozendael et al., 2002); and 3) the sensitivity of this technique peaks at the instrument altitude and decreases with increasing altitude. Recent advances with testing stratospheric BrO profiles in atmospheric models (Liang et al., 2014) provide opportunities to properly account for #1 by assimilating information from atmospheric models. Further, retrievals that avoid SZA larger $70^o$ do not suffer from #2, and certain measurement geometries retain information about the FT. Figure S1 (Supplement) depicts the box Air Mass Factors (bAMFs), which represent the sensitivity of the slant column density (SCD) measurement geometry to BrO concentrations at different altitudes, for two pointing directions (or elevation angles, EA = 25° and 90° upwards) at several SZA; at SZA<70° the sensitivity of these EAs peaks between 2-15km. A more comprehensive view of the bAMFs for different EAs over a wider SZA range is shown in Figure S2 (Supplement).

Van Roozendael et al. (2002) compared ground-based and balloon-borne measurements to VCDs of BrO from the space-borne Global Ozone Monitoring Experiment (GOME) and found all platforms were consistent with a rather widespread tropospheric BrO VCD of $1\text{-}3\text{x}10^{13}$ molec $cm^{-2}$ once appropriate radiative transfer effects were taken into consideration. Salawitch et al. (2005) and Theys et al. (2011) also report satellite derived tropospheric BrO VCDs (GOME and GOME-2, respectively) for the mid-latitudes of $2\text{x}10^{13}$ molec $cm^{-2}$ and $1\text{-}3\text{x}10^{13}$ molec $cm^{-2}$, respectively. Ground based measurements (Theys et al. 2007; Coburn et al., 2011) in the mid-latitudes have reported BrO VCDs of $1\text{-}2\text{x}10^{13}$ molec $cm^{-2}$ that are comparable to the findings

from satellites. Volkamer et al. (2015) recently reported 1.6x$10^{13}$ molec $cm^{-2}$ BrO VCD in the tropics measured by limb-observations from aircraft. All of these studies point to the widespread presence of BrO in the FT, corresponding to a VCD of 1-3x$10^{13}$ molec $cm^{-2}$. Based on these reports, tropospheric BrO could account for 20-30% of a total BrO VCD ~5-6x$10^{13}$ molec $cm^{-2}$ as seen from satellite (van Roozendael et al., 2002; Theys et al., 2011), and significantly impact the lifetime of tropospheric $O_3$ and atmospheric GEM (Wang et al., 2015).

### 1.1 Atmospheric Hg in the South Eastern US

Mercury in the atmosphere exists in three forms: gaseous elemental mercury ($Hg^0$, GEM), gaseous oxidized mercury in the form of either $Hg^{2+}$ or $Hg^{1+}$ (GOM), and particle-bound mercury (PBM). Understanding the processes that cycle mercury between its various forms (GEM ↔ GOM ↔ PBM) is of great importance because this speciation controls the deposition of mercury to the environment, i.e, GOM and PBM are more readily removed from the atmosphere via wet and dry deposition than GEM (Lindberg and Stratton 1998; Bullock 2000). Once deposited, biological processes can methylate $Hg^{2+}$ to form the neurotoxin methyl mercury, which bio-accumulates in fish. Enhancement factors for methyl mercury of up to $10^6$ relative to water have been measured in predatory fish tissues (Schroeder and Munthe 1998; Selin et al., 2010).

A better understanding of the processes controlling atmospheric mercury oxidation, and therewith removal, is particularly relevant for regions that experience high levels of mercury deposition, such as the Southeastern United States. (SE U.S.). Figure 1 shows a map of the Total Mercury Wet Deposition in the US from 2013 (http://nadp.sws.uiuc.edu/maplib/pdf/mdn/hg_dep_2013.pdf). The high deposition levels experienced in the SE U.S. cannot be explained by regional anthropogenic sources of mercury alone, which are mainly located within the Ohio River Valley where the prevailing winds carry emissions northeast. Additionally, several modeling studies (Zhang et al., 2012; Nair et al., 2013) have shown that meteorological patterns above the SE U.S. greatly influence the wet deposition of mercury and that these processes are linked with deep convective activity. This indicates that a regional emission-deposition pattern is most likely not the major source-

receptor relationship for mercury entering the environment over Florida, in the SE U.S., meaning that other possibilities, such as enhanced atmospheric oxidation followed by deposition, need to be explored.

## 2 Experimental

### 2.1 Atmospheric Conditions

The case study during 9 April 2010 provided optimal conditions for assessing the ability of a ground-based MAX-DOAS instrument to measure FT trace gases (see Sect. S1 Supplement for a brief overview of instrumentation and measurement site). Figure 2 shows a time series of trace gas differential slant column densities (dSCD) of BrO, IO, $NO_2$, and $O_4$ for the week surrounding the case study day; with 9 April highlighted by the blue box. The IO measurements are assimilated and used in the modeling portion of this study (Sect. 3.4), while the $NO_2$ measurements give an indication on the amount of influence from anthropogenic activities in the lowest layers of the BL. This day provides an excellent case study for two reasons: 1) consistent shape of the $O_4$ dSCDs across elevation angles as well as the clear splitting between the values is a good indicator for a cloud-free day, and 2) the relatively high $O_4$ dSCDs values (compared with other days) indicates a low aerosol load, enabling the instrument to realize longer light paths (increased sensitivity due to fewer extinction events), and an unobstructed view of the FT. An inspection of webcam pictures for the instrument site proved the day to be free of visual clouds, and precursory look at the aerosol load confirmed the low values. Figure 2 also contains in-situ $O_3$ measurements (from both the US EPA site and a nearby Mercury Deposition Network (MDN) site), oxidized mercury measurements (see below), as well as wind direction measurements from a WeatherFlow, Inc. monitoring station located in Gulf Breeze, FL near the US EPA site.

Oxidized mercury measurements ($Hg^{II}$ = GOM+PBM) at the Pensacola MDN site during study period (see Edgerton et al., 2006 for a detailed description of the site and instrumentation) are also shown in the bottom panel of Fig. 2 (also Fig. 9, Sect. 3.4). On 9 April, $Hg^{II}$ concentrations at the MDN site were rising from near zero on 8 April (due to rain) to peak values of 15-40 pg $m^{-3}$ on the following days, which is above average for the season. In prior years, average daily peak

concentrations at this site in spring were 15 pg $m^{-3}$, which is higher than during any other season (Weiss-Penzias et al., 2011; Nair et al., 2012). Observed GEM concentrations are persistently around 1.4 ng $m^{-3}$ throughout early April, as expected for this season, and therefore not shown. It should be noted, that recent studies have found that measurements of $Hg^{II}$ using KCl denuders can be influenced by atmospheric conditions and other trace gases (McClure et al., 2014) and these external factors can lead to an underestimation of $Hg^{II}$.

## 2.2 External Model Overview

The Whole Atmosphere Community Climate Model version 4 (WACCM4) (Garcia et al., 2007; Marsh et al., 2013) has been extensively evaluated for its representation of the stratosphere, including stratospheric BrO (SPARC CCMVal, 2010). The model does not represent tropospheric bromine sources from very short lived species (VSLS, bromocarbons); and using this model in this study is an active choice to assure a-priori information about tropospheric BrO represents a lower limit (see Sect. 2.4.1). However, $CHBr_3$ and $CH_2Br_2$ concentrations are fixed at the cold point and add about 5-6 pptv stratospheric $Br_y$ (stratospheric $Br_y$ loading is 21-22pptv). In this work, WACCM is run with specified (external) meteorological fields. This is achieved by relaxing the horizontal winds and temperatures to reanalysis fields. The reanalysis fields used are taken from the NASA Global Modeling and Assimilation Office (GMAO) Modern-Era Retrospective Analysis for Research and Applications (MERRA) (Rienecker, et al., 2011). The horizontal resolution is 1.9° x 2.5° (latitude x longitude), with 88 vertical levels from the surface to the lower thermosphere (~140 km). Other WACCM model outputs used are: HCHO, temperature, and pressure vertical profiles. Time synchronized BrO vertical profiles from WACCM are used as a-priori inputs to the inversion (tropospheric VCDs ~$1x10^{13}$ molec $cm^{-2}$), while HCHO profiles are used as input for the box model utilized in this study (see Sect. S4 Supplement). Temperature and pressure profiles were used to construct a molecular density profile in order to convert from concentration (output units of the inversion) to volume mixing ratios (VMR). Model data was generated specifically for this case study in order to best represent that atmospheric composition at the time of the measurements.

The GEOS-Chem global chemical transport model is used to provide a regional and seasonal context for the DOAS observations and their relevance to mercury chemistry. GEOS-Chem (v9-02, www.geos-chem.org) is driven by assimilated meteorology from the NASA Goddard Earth Observing System (GEOS-5). Simulations here have 2° × 2.5° horizontal resolution at 47 vertical layers for bromine and all species except mercury, which have 4° × 5° horizontal resolution. The bromine chemical mechanism, described by Parrella et al. (2012), includes marine bromocarbon emissions from Liang et al. (2010) and debromination of sea salt aerosols (Sander et al., 2003; Yang et al., 2005). Tropospheric bromine concentrations from GEOS-Chem are merged with stratospheric bromine from GEOS-CCM (Liang et al., 2010) to produce a complete atmospheric column (tropospheric VCD of $1.5 \times 10^{13}$ molec $cm^{-2}$). The GEOS-Chem BrO vertical profile is also used as input to the box model in order to assess sensitivity to differences between measured and modeled BrO vertical distributions on mercury oxidation; GEOS-Chem $O_3$ and $NO_2$ profiles are also used as input to the box model. Additionally, the GEOS-CCM profile is utilized as an a-priori during the inversion of the MAX-DOAS measurements due to its representation of the stratosphere while excluding most bromine chemistry in the troposphere (lower limit of bromine in the FT, tropospheric VCD of $3.5 \times 10^{12}$ molec $cm^{-2}$). The mercury simulation is configured as described by Zhang et al. (2012), which includes GEM and two $Hg^{II}$ species: GOM and PBM. Anthropogenic mercury emissions are from the US EPA National Emission Inventory (NEI) 2005 and National Pollutant Release Inventory (NPRI) 2005 inventories over North America (Zhang et al., 2012), which are adjusted to account for $Hg^{II}$ reduction in power plant plumes (Landis et al., 2014), and elsewhere from the Global Emission Inventory Activity (GEIA) (Streets et al. 2009; Corbitt et al., 2011). Emissions and cycling from oceans and the biosphere are also included (Selin et al., 2008; Soerensen et al., 2010). Atmospheric GEM is oxidized by bromine (Holmes et al., 2010) using updated kinetic rate coefficients from Goodsite et al. (2012) and bromine concentrations from GEOS-Chem. $Hg^{II}$ partitions between GOM and PBM (Rutter et al., 2007; Amos et al., 2012) which are both quickly scavenged by precipitation or dry deposited, but also susceptible to reduction in cloud water. The bromine and mercury simulations are both spun up for at least one year. The model is then sampled hourly during April 2010 over Pensacola.

225

226 ## 2.3 DOAS BrO Retrieval

227 Following is a brief description of the parameters and settings used for the DOAS analysis of
228 BrO for this study. A series of sensitivity studies on the BrO retrieval determined the optimal
229 wavelength window for the analysis in this study to be 338-359 nm and include a $5^{th}$ order
230 polynomial. Sensitivity studies which varied the fit window, polynomial order, and intensity
231 offset indicate that the chosen fit settings estimate BrO dSCDs conservatively, as is discussed in
232 more detail in the Supplement (Sect. S2). The reference cross sections used in the DOAS
233 retrieval (WinDOAS software, Fayt and van Roozendael, 2001) were: $O_3$ (at 223 and 243 K,
234 Bogumil et al., 2003), $NO_2$ (at 220 and 297 K, Vandaele et al., 1998), $O_4$ (at 293 K, Thalman and
235 Volkamer 2013), HCHO (Meller and Moortgat 2000), BrO (Wilmouth et al., 1999), and a Ring
236 spectrum (Chance and Spurr 1997) calculated using the software DOASIS (Kraus 2006) at 250 K
237 for the reference used in the analysis. Additionally, a constant intensity offset was included in
238 the fit, but limited to a range ($\pm 3 \times 10^{-3}$) determined by an estimation of the upper limit for the
239 correction of spectrometer stray light. Details of the retrieval for other traces gases can be
240 found in Table 1 along with an overview of the BrO retrieval settings listed here. A single zenith
241 reference from a low SZA of the case study day was used to analyze all spectra (referred to as a
242 fixed reference analysis); this spectrum was taken at ~18:01 UTC on 9 April 2010 (~23° SZA).

243

244 ## 2.4 Inversion Method

245 The retrieval of the BrO VCDs and vertical profiles for this study is a three-step process: 1)
246 aerosol profiles are determined based on DOAS measurements of $O_4$ (see Sect. S3 Supplement);
247 2) derived aerosol profiles are used in a Radiative Transfer Model (RTM) to calculate weighting
248 functions for BrO; and 3) weighing functions are used in an optimal estimation inversion of the
249 DOAS dSCDs to derive VCDs and vertical profiles (Sect. 2.4.1). Additionally, a method is
250 presented here for determining the residual amount of BrO contained in the reference
251 spectrum ($SCD_{Ref}$, Sect. 2.4.2). The relationship between $SCD_{Ref}$ and the measured dSCDs is
252 shown as Eq. (1).

253 $$SCD = dSCD + SCD_{Ref} \quad (1)$$

Both dSCDs and SCDs were used as input to the inversion, and sensitivity tests are presented to assess the impact of the $SCD_{Ref}$ value on the derived vertical profiles and VCDs.

### 2.4.1 Trace Gas Inversion

Weighting functions calculated at 350 nm (for BrO) are used in an optimal estimation (OE) inversion (Rodgers 2000) to determine the trace gas vertical profiles from the MAX-DOAS dSCD measurements, as given by Eq. (2).

$$x_r = x_a + A(x_t - x_a) \quad (2)$$

Here $x_r$ represents the retrieved profile, $x_a$ is the a-priori profile assumption, $A$ is the averaging kernel matrix (AVK), and $x_t$ is the true atmospheric state (represented by the MAX-DOAS dSCD or SCD measurements here). The AVK gives an indication of where the information in $x_r$ is coming from, i.e. information from $x_t$ (measurements) vs $x_a$ (a-priori assumption). The trace of this matrix gives the degrees of freedom (DoF) of the retrieval and indicates how many independent pieces of information are contained in the retrieval (see Sect. 3.1).

One important aspect in this study is the choice of the altitude grid used for both the radiative transfer calculations and the inversion. We used a grid of varying layer thickness: 0.5 km from 0-2 km; a single 3 km layer from 2-5km, and 5 km layer thickness from 5-50 km. This grid is chosen to effectively combine the information from multiple altitudes into a single grid point to assure reasonable peaks in the averaging kernels at increasing altitude, where the MAX-DOAS measurements have limited vertical resolution.

For the BrO inversion, four different a-priori profiles are used in order to assess the robustness of the inversion (see Fig. 5 Sect. 3.2, which shows three of the a-priori profiles along with their corresponding a-posteriori results). Two of the a-priori profiles are based on WACCM model output, the third used data from the CU Airborne-MAX-DOAS (AMAX-DOAS) instrument collected during the Tropical Ocean tRoposphere Exchange of Reactive halogen species and Oxygenated VOC (TORERO) 2012 field campaign (Volkamer et al., 2015), and the fourth is a mean profile from GEOS-CCM. The a-priori profiles from WACCM are: 1) direct model output for the time of each MAX-DOAS scan throughout the day (i.e., different a-priori profile for each MAX-DOAS scan); and 2) the profiles from 1) increased by 40% (in VMR space). The a-priori profile for the TORERO case is derived from data collected during research flight 12 (RF12,

Volkamer et al., 2015), which closely represents also the tropical average BrO profile (see Fig. 2 in Wang et al., 2015). The GEOS-CCM profile is a daytime zonal mean at 30° N. The TORERO and GEOS-CCM profiles are used to invert each MAX-DOAS scan, i.e., the same profile is used for each scan inversion. This is in contrast to the WACCM a-priori profiles, which change throughout the day, due to the availability of time resolved output. For reference, diurnal variations in the WACCM model output for BrO vertical distributions are shown in Fig. S3 (Supplement) panel (a), while panel (b) shows the corresponding tropospheric and total VCDs from these profiles. The a-priori profile error used as input to the OE is constructed based on upper limit values (in units of VMR) expected throughout the troposphere; this is set at 1 pptv for altitudes 0-2 km, 3 pptv for 2-5 km, and 4 pptv for 5-20km (except for the GEOS-CCM case where this altitude range is set to 6 pptv to account for the extremely low values found in the lower FT of the a-priori). The a-priori error is constrained to 40% for the stratospheric portion of the profile (20-50 km), based on the assumption that the WACCM and GEOS-CCM profiles in this region of the atmosphere accurately represent the true atmospheric state, but allowing for sufficient room to reflect contributions of very short-lived organo halogen species (VSLS) to stratospheric BrO (Liang et al., 2014).

A similar method is also used to derive IO profiles (used as input to the modeling in Sect. 3.4). The IO inversion uses two a-priori profiles: 1) a moderate IO VMR in the BL (0.2 - 0.5 pptv) and decreasing to very low levels (<0.1 pptv) throughout the rest of the troposphere; and 2) profiles from recently reported AMAX-DOAS measurements (Dix et al., 2013; Volkamer et al., 2015). A summary of the a-priori profiles, example a-posteriori profiles, the average (for the case study) profile, and the diurnal variation in the VCD for IO is found is Fig. S4 (Supplement).

### 2.4.2 Determination of $SCD_{Ref}$

The BrO profile at the recording time of the fixed reference spectrum is included in the analysis by estimating the reference SCD ($SCD_{Ref}$) for BrO, which is then added to the dSCDs at off-axis EAs according to Eq. (1). Initial sensitivity studies revealed that some MAX-DOAS scans from the case study day are better suited for producing consistent values for $SCD_{Ref}$ than others. The final choice of the reference spectrum is informed from comparing the $SCD_{Ref}$ determined using the iterative method presented here to the $SCD_{Ref}$ predicted by the WACCM a-priori profile 2) (see

Sect. 2.4.1), which assumes a median BrO abundance. The ratio of $SCD_{Ref}$ divided by the BrO VCD corresponds to the AMF of the reference spectrum, which in the case of our case study was ~1.2. The following criteria are applied to select a reference spectrum: (1) the $SCD_{Ref}$ needs to be consistent with the AMF for the a-posteriori BrO profile, as well as (2) be within $\pm 1 \times 10^{13}$ molec $cm^{-2}$ of the WACCM profile increased by 40% (see Sect. 2.4.1). Figure S5 (Supplement) shows the results from this approach for multiple zenith spectra (potential references) on the case study day, and thus illustrates the need for active measures, such as the above, to build internal consistency between the BrO $SCD_{Ref}$, BrO VCD, AMF, and forward RTM calculations of the a-priori and a-posteriori BrO profiles. The results presented in this paper are produced from a single reference spectrum (see Sect. 2.3); however, other references that pass the above quality assurance criteria would not alter our conclusions. Selecting another reference spectrum that meets the aforementioned criteria only increases the variability in the derived VCD by less than $9 \times 10^{12}$ molec $cm^{-2}$ (for any given single scan), and changing the a-priori assumption has also only a small effect on the VCDs ($\pm 1.5 \times 10^{12}$ molec $cm^{-2}$ from average value).

**Iterative Approach:** The value of $SCD_{Ref}$ is determined here by iteratively running the optimal estimation inversion on the MAX-DOAS scan containing the reference spectrum; this process is shown as flow chart in Fig. 3 panel (a). The initial value for $SCD_{Ref}$ is determined from the a-priori profile, and subsequent $SCD_{Ref}$ values are determined from the a-posteriori profile of the inversion returned from the previous iteration. For each iteration only $SCD_{Ref}$ changes; the a-priori profile remains constant. After multiple iterations this method converges on a $SCD_{Ref}$ that minimizes the differences between the measured and forward calculated scan SCD inputs. This value is then used as input for the inversion of the rest of the MAX-DOAS scans throughout the day. Figure 3 panel (b) depicts the iterative refinement of the $SCD_{Ref}$ and corresponding VCD for the reference chosen as most ideal for this case study.

# 3 Results and Discussion

## 3.1 Characterizing the BrO profile retrieval

Figure 4 compares the AVK resulting from the OE inversion of BrO SCDs constructed by accounting for $SCD_{Ref}$ (addition of this value to the measured dSCD output from the DOAS

analysis prior to inversion) vs not accounting for $SCD_{Ref}$ (where SCD = dSCD and with appropriate modification of the weighting functions to reflect this treatment). The largest differences are seen at low SZA in the FT. Panel (a) shows the AVK matrix, which gives an indication as to how much information can be derived from the measurements at specific altitudes, as a function of altitude for the inversion (at SZA = 25°) accounting for $SCD_{Ref}$ (different colored thin lines) along with the diagonal of this matrix (thick black line) and the diagonal for the inversion not accounting for $SCD_{Ref}$ (thick red line). Panel (b) of Fig. 4 shows the difference between the two diagonals as a function of altitude. Also listed in Fig. 4 are DoFs for the different retrieval methods, which, when $SCD_{Ref}$ is properly accounted for, demonstrate an increase of 0.5 (mostly coming from the FT). For these reasons, we chose to include $SCD_{Ref}$ in the inversion of the measured BrO dSCDs in order to further maximize the sensitivity of these measurements towards the FT. Additional information on the DoFs and inversion RMS for these retrievals throughout the case study day are found in Fig. S6 (Supplement). It should be noted that the presence of even moderate aerosol loads would significantly impact the ability to derive vertical profiles extending into the FT, but column integrated information would remain intact.

Recently, Volkamer et al. (2015) reported significant sensitivity of ship MAX-DOAS profiles to the magnitude of $SCD_{Ref}$ over oceans. For several case studies independent aircraft measurements above the ship show that a significant trace gas partial column resides above the BL (IO and glyoxal). They find that while the BL VMR is insensitive to the value of $SCD_{Ref}$, the partial tropospheric VCD can be impacted by up to a factor of 2-3. During this study the impact of using BrO dSCDs, rather than SCDs, in the inversion lead to an average percent difference in the BrO VCD derived for each MAX-DOAS scan of ~30%. The average VCDs were $2.1 \times 10^{13}$ and $2.3 \times 10^{13}$ molec $cm^{-2}$ (integrated from 0-15 km) when using dSCDs or SCDs (only ~10% difference). This reflects that the inversion based on dSCDs (not accounting for $SCD_{Ref}$) produced highly variable FT VCDs throughout the case study day, and that this variability is reduced for the SCD based inversion.

The reduced variability in the BrO VCD compared to the other gases investigated by Volkamer et al. (2015) is probably due to the fact that no BrO was detected in the BL in either case study.

For glyoxal and IO about 50% of the VCD resides near the instrument altitude (Volkamer et al., 2015). This BL contribution adds offsets to the SCDs also for the higher EAs that 'partially obstruct' the view of the FT, and makes FT partial columns subject to larger error bars. The lack of BrO in the BL seems to simplify measurements of FT partial columns from the ground. The Volkamer et al. case studies in combination with our results thus suggest that MAX-DOAS instruments that are to measure FT partial columns of gases other than BrO should actively avoid complications from absorbers near instrument altitude, for example by placing the instrument on mountaintops. The lack of aerosols from high mountaintops has the additional benefit of increased sensitivity to measure profiles for BrO and other gases.

### 3.2 BrO VCDs and Vertical Profiles

Figure 5 shows the results from the inversions using the three different a-priori profiles. Panel (a) shows the a-priori profiles, and the a-posteriori vertical profiles corresponding to one scan at ~23° SZA (around solar noon), as well as the median profile from all profiles. A total of 45 profiles, corresponding to SZA<70° for each a-priori case, were combined to create the median BrO vertical profile for the case study day (Fig. 5). The median profile was used for the modeling results and discussion in Sect. 3.4. Panel (b) shows the AVK (see Sect. 2.4.1) from the inversion using the un-modified WACCM BrO output as the a-priori profile. In an ideal scenario, the AVK for each layer peaks near unity within that layer. The derived vertical profiles show only slight dependence on the a-priori profile with a maximum average difference between a-posteriori profiles of ~0.6 ppt at altitudes <15km for the entire day. These profile differences have only a small effect on the free tropospheric VCDs, i.e. <20% difference for SZA<70°. The AVK peaks twice – once in the lowest layer (from the lowest looking elevation angles) and again between 5km and 20km, which reflects the combination of the optimization of the radiative transfer grid and the measurement sensitivity. This is interpreted as an indication that the DoFs remaining after accounting for the peak at instrument altitude correspond to the FT. Figure S7 (Supplement) contains a comparison of the a-posteriori profile derived BrO dSCDs and the measured dSCDs (panels a and b) and the corresponding RMS difference between measured and calculated dSCDs in panel (c).

This inversion procedure allows for the determination of the diurnal variation in the BL (0-1km), FT (1-15km), and total VCDs for BrO. These results, corresponding to the inversion utilizing WACCM output as the a-priori profile, are found in Fig. 6 panel (b) along with the corresponding DoFs panel (a). The errors bars on the tropospheric and stratospheric VCDs reflect the range of derived values resulting from the use of different a-priori assumptions. The retrieved diurnal variation in the free tropospheric (1-15 km) BrO VCD follows that of the total VCD with an average of 53% contribution to the total and varying between 47-57% throughout the day; this corresponds to a daytime average VCD of ~2.3±0.16x$10^{13}$ molec $cm^{-2}$, where the error reflects the average error on the VCD as seen in Fig. 6 panel (b). The overall error on the average VCD is ~0.7x$10^{13}$ molec $cm^{-2}$ and takes into account change in the VCD when assuming the maximum profile error given by the OE inversion. This treatment is expressed in Eq. (3).

$$Total\ Error = \frac{(VCD_{Prf} - VCD_{Prf+OE\ err})}{2} \quad (3)$$

where $VCD_{Prf}$ is the VCD calculated directly from the OE inversion a-posteriori, $VCD_{Prf+OE\ err}$ is the VCD calculated from the OE inversion a-posteriori profile plus the OE error of that profile, and the factor of 2 reflects that the OE inversion error at each altitude covers oscillations both higher and lower than the retrieved profile at that point.

The tropospheric VCD of ~2.3±0.7x$10^{13}$ molec $cm^{-2}$ BrO derived from this study falls in the range of other currently reported measurements, which span from ~1-3x$10^{13}$ molec $cm^{-2}$ (van Roozendael et al., 2002; Salawitch et al., 2005; Theys et al., 2007; Theys et al., 2011; Coburn et al., 2011; Volkamer et al., 2015; Wang et al., 2015). The observed tropospheric BrO VCD is consistent with the VCD of 2.0x$10^{13}$ molec $cm^{-2}$ measured by the same instrument during a previous study in the same location (Coburn et al., 2011). This value is higher than other ground based measurements in the Southern Hemisphere tropics (Theys et al., 2007), which reported tropospheric VCDs of 1.1-1.2x$10^{13}$ molec $cm^{-2}$. Aircraft profiles over the Pacific ocean have reported variable BrO VCDs ranging from 1.0 to 1.7 x$10^{13}$ molec $cm^{-2}$ BrO, and a campaign average of 1.3±0.2x$10^{13}$ molec $cm^{-2}$ BrO (Volkamer et al., 2015; Wang et al., 2015). While it appears that the BrO VCD is highly variable, depending on the location and time of measurement, the average BrO VCD measured by the GOME-2 (Global Ozone Monitoring

Experiment-2) satellite for Jan/Feb in the tropics (30N – 30S; longitudinal average) is 1.6 x$10^{13}$ molec $cm^{-2}$, in reasonably close agreement with ground- and aircraft studies. Much of the current knowledge of bromine chemistry in the upper troposphere–lower stratosphere (UTLS) is currently based on balloon-borne direct-sun BrO measurements (Pundt et al., 2002; Dorf et al., 2008), which have found an order of magnitude lower BrO. This lower BrO is – at least in part – due to atmospheric variability (see e.g., Wang et al., 2015; Schmidt et al., 2016). Ground-, aircraft- and satellite measurements consistently support elevated BrO in the FT. A re-assessment of halogen chemistry in the UTLS (bromine and iodine) seems warranted (Volkamer et al., 2015; Wang et al., 2015; Saiz-Lopez et al., 2015).

### 3.3 Comparison with models

Global model results for BrO VCDs generally predict much lower columns than observed in this study. Yang et al. (2005), using the p-TOMCAT model, found mid-latitudes values of ~0.4x$10^{13}$ molec $cm^{-2}$ for spring/summer months; and Parrella et al. (2012), using GEOS-Chem, reported values of <1x$10^{13}$ molec $cm^{-2}$ for the entire year for the Northern Hemisphere mid-latitudes. The value from Parella et al. (2012) is slightly more comparable to that predicted by WACCM for the case study day (~1x$10^{13}$ molec $cm^{-2}$, see Fig. S3, Supplement). Wang et al. (2015) reported sensitivity in the predicted BrO to updated heterogeneous chemistry of bromine (Ammann et al., 2013). Recently, Schmidt et al., (2016, in press) has incorporated the Enhanced Heterogeneous Chemistry (EHC) scheme into GEOS-Chem. The EHC bromine chemistry mechanism produces higher average tropospheric BrO columns, which are more consistent with our observations. They site that average tropospheric BrO concentrations are ~50% more than predicted from the Parrella et al., (2012) bromine mechanism; this is similar to the findings from this study where the tropospheric VCD predicted by GEOS-Chem (which uses the Parrella et al., (2012) bromine chemistry) is ~30% lower than the measured VCD. Notably, different representations of halogen chemistry can result in very different BrO vertical profile shapes (Sander et al., 2003; Fernandez et al., 2014; Long et al., 2014; Liang et al., 2014) despite an apparently good agreement (~1x$10^{13}$ molec $cm^{-2}$) in the BrO VCD at tropical latitudes. The

ability to predict BrO vertical profiles is particularly relevant to predict distributions of oxidized mercury in the lower troposphere (see Sect. 3.4.2).

## 3.4 Mercury Modeling

A detailed description of the box model utilized in this study to assess the oxidation pathways of mercury is found in the Supplement (Sect. S4). Table 2 gives an overview of the reactions controlling the cycling of atmospheric mercury included in the box model and Fig. S8 (Supplement) contains the vertical profiles of modeled and measured parameters used as input to the box model. In general, the mercury modeling scheme employed in this study follows that as set forth in previous works (Selin et al., 2007; Holmes et al., 2009, 2010; Wang et al., 2015).

### 3.4.1 Mercury oxidation rates

The primary finding from a comparison of the $Hg^0$ oxidation rates for the two radical species tested in this study (Br and $O_3$) is that the reaction with Br dominates the overall rate throughout the troposphere for the conditions tested by this case study, independent of initial BrO vertical profile used. The column integral rate is $7.8 \times 10^4$ molec $cm^{-2}$ $s^{-1}$ for $O_3$; while the Br rates are $3.5 \times 10^5$ and $3.7 \times 10^5$ molec $cm^{-2}$ $s^{-1}$ for the BrO vertical profiles from the MAX-DOAS measurements and GEOS-Chem respectively. Preliminary tests included chlorine (Cl) radicals as an additional oxidant using a vertical distribution estimated for the tropical troposphere (Wang et al., 2015). However, this reaction was deemed unimportant, and is thus not included here, due to the column integral oxidation rates being factors of 18 and 5 lower than column rates for Br and $O_3$, respectively. The reaction rates from Br are at least a factor of 3 greater than the contribution from $O_3$.

The vertically resolved rates are shown in Fig. 7 (panel a) for both reactions: Br (solid blue and dotted pink traces representing the BrO profiles from the MAX-DOAS measurements and GEOS-Chem, respectively, used to derive the Br radical concentrations) and $O_3$ (red trace); reflecting the contributions of these reactions at different altitudes. Also included in Fig. 7 (panel b) are the corresponding lifetimes of GEM (as a function of altitude) against oxidation by the two molecules. Only in the lowest layers of the atmosphere do the rates of oxidation through reaction with $O_3$ become comparable or greater than those of the reaction with Br. However, it

should be noted that for altitudes <4 km where the rate of reaction with $O_3$ dominates, the BrO VMR is <0.03 pptv while the $O_3$ VMR is ~50 ppbv, and in cases where reaction with Br dominates (still at altitudes <4 km) the BrO VMR is still <0.3 pptv. The BrO vertical profile from the MAX-DOAS instrument below 4 km contains the highest amount of uncertainty because BrO is essentially zero within the variability of the measurements. The column integral rates of oxidation based on the MAX-DOAS measurements and the BrO profile from GEOS-Chem are actually quite similar (only ~5% difference), which is most likely due to the additional bromine chemistry included in this model (see Sect. 2.2) as compared to other models (e.g. GEOS-CCM); however, the discrepancies in the vertical distribution of BrO lead to a mismatch in the altitudes at which the oxidation can occur. For both BrO profiles, the reaction with Br dominates above 4 km (indicated by the black dashed line in Fig. 7). Altitudes above 4km are responsible for ~72% of the column integral rate of GEM oxidation (through reaction with Br) based on the MAX-DOAS measurements; while that value decreases to ~56% for the bromine profile from GEOS-Chem.

Additional differences between column oxidation rates for the MAX-DOAS and GEOS-Chem BrO profiles exists at altitudes <4km, where the MAX-DOAS measurements find no BrO and GEOS-Chem predicts up to 0.75 pptv. Similar to the findings of this study, other publications have put upper limits on marine boundary layer (MBL) BrO ~0.5 pptv, (Gomez-Martin et al., 2013; Wang et al., 2015; Volkamer et al., 2015).

### 3.4.2 Mercury oxidation pathways

Figure 8 shows the results of the "traditional" (panel a) and "revised" (panel b) HgBr scavenging schemes (see Sect. S4 Supplement for descriptions) on the rate of GEM oxidation as a function of altitude. In each panel, contributions of individual molecules (colored lines) are shown along with the total removal rate (black lines). Panel (c) shows the vertical profile of the ratio of the "revised" total rate to "traditional" total rate, which demonstrates the enhanced oxidation of HgBr when considering the additional scavenging reactions. In the "traditional" model the percent contributions to the column integrated rate of oxidation of HgBr are 57.5% and 42.5% for OH and Br, respectively; and in the "revised" model the percent contributions are as follows: 71.3% ($NO_2$); 21.3% ($HO_2$); 4.3% (BrO); 1.4% (OH); 1.1% (Br); 0.5% (IO); and <0.1% (I).

Note that mercury oxidation is initiated by reaction between Br radicals and GEM in both reaction schemes, and the additional scavenging reactions in the "revised" scheme primarily increase the overall rate of oxidation at altitudes where HgBr decomposition is fast. The greatest enhancement is seen below 8 km, where the overall rate of oxidation is ~100 times faster, primarily because of the reaction of HgBr with $NO_2$ and $HO_2$.

Figure 8 also illustrates the increased number of species produced from the additional oxidation mechanisms, some of which may have physical and chemical properties that differ from the two products of the "traditional" mode, which are also products in the "revised" scenario but are present at much lower concentrations. In the "traditional" scenario at 1 km, the scavenging products HgBrOH and $HgBr_2$ account for 96% and 4% of the total HgBrX, respectively, and these values drop to 0.5% and <<0.1% in the "revised" scenario where $HgBrNO_2$ accounts for 73% of HgBrX. In the "revised" scenario, $HgBrNO_2$ remains the major product throughout the atmosphere, but at free tropospheric altitudes $HgBrHO_2$ also contributes significantly at 37%, compared to $HgBrNO_2$ at 52%. There are currently no observations of the molecular composition of GOM with which to evaluate these simulated product distributions.

### 3.4.3 Mercury lifetime with respect to oxidation

The above oxidation rates correspond to a minimum lifetime of GEM with respect to oxidation by bromine radicals of ~20 days in the FT (based on the MAX-DOAS measurements). The average total ($Hg^0$ + Br and $Hg^0$ + $O_3$) tropospheric column lifetimes are 38 and 54 days (altitudes >4 km) for the scenarios including BrO profiles from the MAX-DOAS measurements and GEOS-Chem, respectively; where in both cases the contribution from the reactions with $O_3$ are the same and the differences are owing to the differing amounts of Br radicals. This is much shorter than the currently expected atmospheric lifetime on the order of several months. However, the box model only accounts for partitioning of the GOM species between the gas phase and aerosols; once they are in the aqueous phase they can be photo-reduced to GEM that can then subsequently return to the gas phase (Costa and Liss, 1999), thus extending the effective lifetime significantly beyond that calculated above. The kinetic coefficients for reactions involving HgBr come mainly from quantum chemical calculations, which have

543 significant uncertainties, so the simulated GEM lifetime could be extended by reducing the rate
544 coefficients within their uncertainties. Another possible mechanism is the photo-dissociation of
545 HgBrX products containing species that have significant absorption cross-sections in the ultra-
546 violet/visible (UV/Vis) region of the electromagnetic radiation spectrum, e.g. $HgBrNO_2$,
547 $HgBrHO_2$, which could reproduce HgBr. This HgBr could then thermally decompose to re-form
548 GEM, or be oxidized again. Our observations are consistent with previous findings (Wang et al.,
549 2015), that establish GEM as a chemically highly dynamic component of the FT. It is expected
550 that GOM species will go through additional processes also in the aqueous phase, which could
551 significantly impact the ultimate fate of the mercury.
552
553 **3.5 Atmospheric Implications**
554 The rapid oxidation of mercury in the lower FT is of potential relevance in the SE U.S., where
555 there have been several studies linking deep convective activity to the elevated levels of
556 mercury found in rainwater (Guentzel et al., 2001; Landing et al., 2010; Nair et al., 2013). The
557 bio-accumulation of methyl mercury in fish tissues is particularly relevant in this region, where
558 it has been deemed unsafe to eat fish harvested from many lakes in the region (Engle et al.,
559 2008; Liu et al., 2008). Wet deposition measurements of mercury exceed what can be explained
560 through regional sources in the southeast. In fact, Guentzel et al., (2001) estimated that <46%
561 of the mercury deposited in Florida was a result of local emissions, the other >50% was
562 attributed to long-range transport of mercury in the atmosphere; the transported fraction may
563 have increased since those data were collected in the 1990s because regional US mercury
564 emissions have declined while global emissions have risen. This attribution, coupled with
565 mountaintop and aircraft studies locating elevated levels of GOM in the FT (Swartzendruber et
566 al., 2006; Faïn et al., 2009; Swartzendruber et al., 2009; Lyman and Jaffe 2012; Brooks et al.,
567 2014; Weiss-Penzias et al., 2015, Shah et al., 2016), strongly suggests the presence of a global
568 "pool" of mercury in the upper atmosphere that contributes to widespread mercury deposition
569 on a local to regional scale.
570 On the case study day, $Hg^{II}$ (=GOM+PBM) concentrations at the nearly Pensacola MDN site
571 reached 25 pg $m^{-3}$ around midday and nearly 40 pg $m^{-3}$ on 10 April (Fig. 9). High $Hg^{II}$ events in

572 Pensacola are frequently consistent with emissions from a nearby coal-fired power plant,
573 however about 25% of such events have significant contributions from the FT (Weiss-Penzias et
574 al., 2011). The high $Hg^{II}$:$SO_2$ ratios (10-20 pg $m^{-3}$ $ppb^{-1}$) and high $NO_y$:$SO_2$ ratios (3.5-5.2 ppb $ppb^{-1}$)
575 recorded on 9-10 April make the power plant an unlikely source of the $Hg^{II}$ on these days (Fig.
576 S9, Supplement); for comparison, Weiss-Penzias et al. (2011) reported $Hg^{II}$:$SO_2$ and $NO_y$:$SO_2$
577 ratios of 3.5 and 1.0, respectively, in power plant plumes. Like $Hg^{II}$ concentrations, ozone
578 concentrations and $Hg^{II}$ dry deposition in Florida also peak in spring, all of which are consistent
579 with a significant source of surface $Hg^{II}$ being from the upper troposphere (Lyman et al., 2009;
580 Gustin et al., 2012). We use the GEOS-Chem model to further probe the sources of this $Hg^{II}$.
581 Figure 9 shows that the model generally reproduces the day-to-day variability of $Hg^{II}$
582 observations during April 2010 (but not extremes), such as the low concentrations during 7-8
583 April and relative maxima on 5 and 10 April. In both the model and observations, $Hg^{II}$
584 concentrations rise abruptly in the morning, consistent with entrainment of $Hg^{II}$ aloft, and
585 unlike the other combustion tracers (e.g. $NO_y$, $SO_2$) that reach high concentrations at night (Fig.
586 S9, Supplement). The model does not reproduce the abrupt drop in $Hg^{II}$ around 18:00 CST,
587 however, which may be partly due to local sea breeze circulations that are evident in wind
588 observations but not simulated at the 4°x5° model resolution. In addition, mixing depth errors
589 in the driving meteorology are known to affect other species, particularly at night (Lin et al.,
590 2010; McGrath-Spangler and Molod, 2014). To assess the contribution of the FT to surface $Hg^{II}$
591 during April 2010, we conduct an additional model simulation with zero anthropogenic
592 emissions in North America and no mercury redox chemistry in the lower troposphere (> 700
593 hPa). The simulation is initialized from the base run on 1 April. Due to its fast deposition, all
594 boundary-layer $Hg^{II}$ in the sensitivity simulation after about 1 day originates from oxidation of
595 GEM in the free troposphere or, less likely, from intercontinental transport of anthropogenic
596 $Hg^{II}$. Figure 9 shows there is little difference between the base and sensitivity simulations,
597 meaning that the FT is the main source of boundary-layer $Hg^{II}$ in the model and that variability
598 in the FT component explains most of the day-to-day $Hg^{II}$ variability. Thus, the 3-D model shows
599 that conditions on 9 April are favorable for $Hg^{II}$ transport to the boundary layer, exactly when
600 the DOAS observations find substantial amounts of BrO are present in the FT.

601 The GEM oxidation mechanism in the 3-D model corresponds to the "traditional" scheme in the
602 box model and bromine concentrations in GEOS-Chem are lower than recent aircraft
603 observations (Volkamer et al., 2015), so the GEM oxidation may be faster than simulated.
604 Greater $Hg^{II}$ production in the FT might help correct the model's 20% low bias in mercury wet
605 deposition over the Southeast US (Zhang et al., 2012), but this would depend on the rate of any
606 compensating reduction reaction, as discussed above. The findings of this study indicate that
607 the amount of bromine located in the FT can be sufficient to quickly oxidize GEM.
608

609 **4 Conclusions**

610 We show the benefits of determining $SCD_{Ref}$ to maximize the sensitivity of ground based MAX-
611 DOAS measurements to detect BrO in the FT, and improve the overall consistency of time-
612 resolved BrO tropospheric VCDs. The retrieval can also be applied to other trace gases.
613 Knowledge of $SCD_{Ref}$ allows the derivation of one vertical profile for each MAX-DOAS scan
614 throughout the day (SZA<70°) and the assessment of the diurnal variation of the partial BrO
615 vertical columns. Our retrieval is complementary to previous studies that have characterized
616 the stratosphere using zenith-sky measurements under twilight conditions (Theys et al., 2007;
617 Hendrick et al. 2007), and minimizes the influence of $O_3$ absorption, and the contribution of
618 stratospheric BrO to the overall BrO signal by using CTM output to constrain stratospheric BrO
619 in combination with BrO dSCDs measured at low SZA instead. The FT VCDs reported here are in
620 good agreement with the previously cited values for BrO, with the average BrO FT VCD
621 (~$2.3 \times 10^{13}$ molec $cm^{-2}$) falling within the range reported by other studies (1-$3 \times 10^{13}$ molec $cm^{-2}$)
622 (see Wang et al., 2015, and references therein). These measurements all point to the presence
623 of background amounts of BrO in the FT that is larger than current models predict. The method
624 employed here would also benefit from deployments at mountaintop sites where aerosol
625 shielding of the FT can be overcome and tropospheric vertical distributions could be assessed
626 more frequently.
627 The presented box model studies indicate that for the conditions probed bromine radicals are
628 the dominant oxidant for atmospheric GEM throughout the FT above the studied region. Given
629 the similarities between the vertical profiles of BrO derived in this study and other profiles

measured in the tropical FT (Volkamer et al., 2015; Wang et al., 2015) the results from our case study may apply more broadly, though past aircraft and modeling studies have reported significant variability in BrO and $Br_y$ (Wang et al., 2015; Schmidt et al., 2016). The drivers for such variability deserve further investigation. Our results confirm that mercury is rapidly oxidized by bromine, and a chemically highly dynamic species in the atmosphere. The chemical lifetime of GEM is ~45 days in the tropical FT based on calculations and vertical profiles presented in this study; longer GEM global lifetimes should thus be regarded to indicate "effective lifetimes", i.e., are the result of rapid chemical cycling of GOM back to GEM (e.g., photoreduction (Pehkonen and Lin, 1998; Gustin et al., 2002; Tong et al., 2013)). Mercury measurements during our study period show high surface $Hg^{II}$ concentrations that likely originate in the FT, meaning that we have observed substantial BrO columns under conditions favorable for $Hg^{II}$ transport to the boundary layer. Additionally, this study suggests that the experimental observation of elevated GOM in the FT may be linked to our incomplete understanding about tropospheric bromine sources (Swartzendruber et al., 2006; Faïn et al., 2009; Lyman and Jaffe 2012; Wang et al., 2015); and indicate that conditions exist where the amount of bromine located in the FT above the (coastal regions) of the SE U.S. is sufficient to quickly oxidize GEM to GOM. This can then be wet deposited and, as such, can help explain the observed elevated wet deposition pattern in this region. Our results highlight the need to understand BrO vertical profiles in the FT, and represent them in atmospheric models to understand the location where mercury is oxidized in the atmosphere, and is available for wet and dry deposition. More studies are needed to test and represent the bromine sources in atmospheric models, test atmospheric GOM abundances by field data, and clarify the chemical identity, the global distribution, and dry and wet removal processes of GOM.

**Acknowledgements**

S.C. is the recipient of a NASA Earth and Space Science graduate fellowship. The CU MAX-DOAS instrument was developed with support from the EPRI's Technology Innovation program (EP-P27450/C13049). Financial support from EPRI (EP-P32238/C14974), US National Science

Foundation (ATM-0847793, AGS-1104104), and CU Boulder startup funds is gratefully acknowledged.

## References


Aliwell, S.R., van Roozendael, M., Johnston, P.V., Richter, A., Wagner, T., Arlander, D.W., Burrows, J.P., Fish, D.J., Jones, R.L., Tørnkvist, K.K., Lambert, J.-C., Pfeilsticker, K., and Pundt, I.: Analysis of BrO in zenith-sky spectra: An Intercomparison exercise for analysis improvement, ACH 10-1–ACH 10-20, J. Geophys. Res. -Atmos., 107, D14, 10.1029/2001JD000329, 2002.

Ammann, M., Cox, R.A., Crowley, J.N., Jenkin, M.E., Mellouki, A., Rossi., M.J., Troe, J., and Wallington, T.J.: Evaluated kinetic and photochemical data for atmospheric chemistry: Volume VI - heterogeneous reactions with liquid substrates, Atmos. Chem. Phys., 13, 16, 8045-8228, DOI: 10.5194/acp-13-8045-2013, 2013.

Amos, H. M., Jacob, D. J., Holmes, C. D., Fisher, J. A., Wang, Q., Yantosca, R. M., Corbitt, E. S., Galarneau, E., Rutter, A. P., Gustin, M. S., Steffen, A., Schauer, J. J., Graydon, J. A., Louis, V. L. S., Talbot, R. W., Edgerton, E. S., Zhang, Y. and Sunderland, E. M.: Gas-particle partitioning of atmospheric Hg(II) and its effect on global mercury deposition, Atmos. Chem. Phys., 12, 591–603, doi:10.5194/acp-12-591-2012, 2012.

Balabanov, N., Shepler, B., and Peterson, K.: Accurate global potential energy surface and reaction dynamics for the ground state of HgBr2, J. Phys. Chem. A, 109, 8765-8773, 10.1021/jp0534151, 2005.

Bogumil, K., Orphal, J., Homann, T., Voigt, S., Spietz, P., Fleischmann, O., Vogel, A., Hartmann, M., Kromminga, H., Bovensmann, H., Frerick, J., and Burrows, J.: Measurements of molecular absorption spectra with the SCIAMACHY pre-flight model: instrument characterization and reference data for atmospheric remote-sensing in the 230-2380 nm region, J. Photochem. Photobiol. A-Chem., 157, 167-184, 10.1016/S1010-6030(03)00062-5, 2003.

Brooks, S., Ren, X., Cohen, M., Luke, W.T., Kelley, P., Artz, R., Hynes, A., Landing, W., and Martos, B.: Airborne Vertical Profiling of Mercury Speciation near Tullahoma, TN, USA, Atmosphere, 5(3), 557-574, 10.3390/atmos5030557, 2014.

Bullock, O.: Modeling assessment of transport and deposition patterns of anthropogenic mercury air emissions in the United States and Canada, Sci. Total Environ., 259, 145-157, 2000.

Chance, K. and Spurr, R.: Ring effect studies: Rayleigh scattering, including molecular parameters for rotational Raman scattering, and the Fraunhofer spectrum, Appl. Opt., 36, 5224-5230, 10.1364/AO.36.005224, 1997.

Coburn, S., Dix, B., Sinreich, R., and Volkamer, R.: The CU ground MAX-DOAS instrument: characterization of RMS noise limitations and first measurements near Pensacola, FL of BrO, IO, and CHOCHO, Atmos. Meas. Tech., 4, 2421-2439, 10.5194/amt-4-2421-2011, 2011.

Corbitt, E. S., Jacob, D. J., Holmes, C. D., Streets, D. G. and Sunderland, E. M.: Global Source-Receptor Relationships for Mercury Deposition Under Present-Day and 2050 Emissions Scenarios, Environ. Sci. Technol., 45, 24, 10477–10484, doi:10.1021/es202496y, 2011.

Costa, M. and Liss, P.S.: Photoreduction of mercury in seawater and its possible implications for $Hg^0$ air-sea fluxes, Mar. Chem., 68, 1-2, 87-95, 10.1016/S0304-4203(99)00067-5, 1999.

Dibble, T. S., Zelie, M. J., and Mao, H.: Thermodynamics of reactions of ClHg and BrHg radicals with atmospherically abundant free radicals, Atmos. Chem. Phys., 12, 10271-10279, 10.5194/acp-12-10271-2012, 2012.

Dix, B., Baidar, S., Bresch, J. F., Hall, S. R., Schmidt, K. S., Wang, S., and Volkamer, R.: Detection of iodine monoxide in the tropical free troposphere, Proc. Natl. Acad. Sci. U. S. A., 110, 2035-2040, 10.1073/pnas.1212386110, 2013.

Donohoue, D., Bauer, D., Cossairt, B., and Hynes, A.: Temperature and pressure dependent rate coefficients for the reaction of Hg with Br and the reaction of Br with Br: A pulsed laser photolysis-pulsed laser induced fluorescence study, J. Phys. Chem. A, 110, 6623-6632, 10.1021/jp054688j, 2006.

Dorf, M., Boesch, H., Butz, A., Camy-Peyret, C., Chipperfield, M. P., Engel, A., Goutail, F., Grunow, K., Hendrick, F., Hrechanyy, S., Naujokat, B., Pommereau, J. -., van Roozendael, M., Sioris, C., Stroh, F., Weidner, F., and Pfeilsticker, K.: Balloon-borne stratospheric BrO measurements: comparison with Envisat/SCIAMACHY BrO limb profiles, Atmos. Chem. Phys., 6, 2483-2501, 2006.

717 Edgerton, E. S., Hartsell, B. E. and Jansen, J. J.: Mercury speciation in coal-fired power plant
718 plumes observed at three surface sites in the southeastern US, Environ. Sci. Technol., 40,
719 15, 4563–4570, doi:10.1021/es0515607, 2006.
720 Engle, M. A., Tate, M. T., Krabbenhoft, D. P., Kolker, A., Olson, M. L., Edgerton, E. S., DeWild, J.
721 F., and McPherson, A. K.: Characterization and cycling of atmospheric mercury along the
722 central US Gulf Coast, Appl. Geochem., 23, 419-437, 10.1016/j.apgeocliem2007.12.024,
723 2008.
724 Eyring, V., Shepherd, T. G., Waugh, D. W. (Eds.): SPARC CCMVal, SPARC Report on the
725 Evaluation of Chemistry-Climate Models, SPARC Report No. 5, WCRP-132, WMO/TD-No.
726 1526, 2010.
727 Faïn, X., Obrist, D., Hallar, A. G., Mccubbin, I., and Rahn, T.: High levels of reactive gaseous
728 mercury observed at a high elevation research laboratory in the Rocky Mountains, Atmos.
729 Chem. Phys., 9, 8049-8060, doi:10.5194/acp-9-8049-2009, 2009.
730 Fayt, C. and van Roozendael, M.: WinDoas 2.1 – Software User Manual, 2001.
731 Fernandez, R.P., Salawitch, R.J., Kinnison, D.E., Lamarque, J.-F., and Saiz-Lopez., A.: Bromine
732 partitioning in the tropical tropopause layer: implications for stratospheric injection, 14, 24,
733 13391-13410, DOI: 10.5194/acp-14-13391-2014, 2014.
734 Fitzenberger, R., Bösch, H., Camy-Peyret, C., Chipperfield, M.P., Harder, H., Platt, U., Sinnhuber,
735 B.-M., Wagner, T., and Pfeilsticker, K.: First profile measurements of tropospheric BrO,
736 2921-2924, Geophys. Res. Lett., 27, 18, 10.1029/2000GL011531, 2000.
737 Garcia, R. R., Marsh, D. R., Kinnison, D. E., Boville, B. A., and Sassi, F.: Simulation of secular
738 trends in the middle atmosphere, 1950-2003, J. Geophys. Res. -Atmos., 112, D09301,
739 10.1029/2006JD007485, 2007.
740 Goodsite, M.E., Plane, J.M.C., and Skov, H.: A theoretical study of the oxidation of $Hg^0$ to $HgBr_2$
741 in the troposphere, Environ. Sci. Technol., 38, 1772-1776, 10.1021/es034680s, 2004.
742 Goodsite, M. E., Plane, J. M. C., and Skov, H.: Correction to A Theoretical Study of the Oxidation
743 of Hg0 to HgBr2 in the Troposphere, Environ. Sci. Technol., 46, 5262-5262,
744 10.1021/es301201c, 2012.

745 Gomez Martin, J.C., Mahajan, A.S., Hay, T.D., Prados-Roman, C., Ordonez, C., MacDonald, S.M.,
746 Plane, J.M.C., Sorribas, M., Gil, M., Mora, J.F.P., Reyes, M.V.A., Oram, D.E., Leedham, E., and
747 Saiz-Lopez, A.: Iodine chemistry in the eastern Pacific marine boundary layer, J. Geophys.
748 Res.-Atmos., 118, 2, 887-904, doi:10.1002/jgrd.50132, 2013.
749 Gustin, M.S., Biester, H., Kim, C.S.: Investigation of the light-enhanced emission of mercury
750 from naturally enriched substrates, Atmos. Environ., 36, 20, 3241-3254, PII S1352-
751 2310(02)00329-1, doi: 10.1016/S1352-2310(02)00329-1, 2002.
752 Gustin, M. S., Weiss-Penzias, P. S. and Peterson, C.: Investigating sources of gaseous oxidized
753 mercury in dry deposition at three sites across Florida, USA, Atmos. Phys., 12, 19, 9201–
754 9219, doi:10.5194/acp-12-9201-2012-supplement, 2012.
755 Guentzel, J., Landing, W., Gill, G., and Pollman, C.: Processes influencing rainfall deposition of
756 mercury in Florida, Environ. Sci. Technol., 35, 863-873, 10.1021/es.001523+, 2001.
757 Hall, B.: The Gas-Phase Oxidation of Elemental Mercury by Ozone, Water Air Soil Pollut., 80,
758 301-315, 10.1007/BF01189680, 1995.
759 Hendrick, F., van Roozendael, M., Chipperfield, M. P., Dorf, M., Goutail, F., Yang, X., Fayt, C.,
760 Hermans, C., Pfeilsticker, K., Pommereau, J. -., Pyle, J. A., Theys, N., and De Maziere, M.:
761 Retrieval of stratospheric and tropospheric BrO profiles and columns using ground-based
762 zenith-sky DOAS observations at Harestua, 60 degrees N, Atmos. Chem. Phys., 7, 4869-4885,
763 2007.
764 Holmes, C. D., Jacob, D. J., Mason, R. P., and Jaffe, D. A.: Sources and deposition of reactive
765 gaseous mercury in the marine atmosphere, Atmos. Environ., 43, 2278-2285,
766 10.1016/j.atmosenv.2009.01.051, 2009.
767 Holmes, C. D., Jacob, D. J., Corbitt, E. S., Mao, J., Yang, X., Talbot, R. and Slemr, F.: Global
768 atmospheric model for mercury including oxidation by bromine atoms, Atmos. Chem. Phys.,
769 10, 24, 12037–12057, doi:10.5194/acp-10-12037-2010, 2010.
770 Hynes, A., Donohoue, D., Goodsite, M., and Hedgecock, I.: Our current understanding of major
771 chemical and physical processes affecting mercury dynamics in the atmosphere and at the
772 air-water/terrestrial interfaces, *Mercury Fate and Transport in the Global Atmosphere*, eds

773 Mason, R. and Pirrone, N., Springer US, 427-457, 2009.Kraus, S,: DOASIS – A Framework
774 Design for DOAS, Shaker Verlag, University of Heidelberg, Germany, 2006.
775 Landing, W. M., Caffrey, J. M., Nolek, S. D., Gosnell, K. J., and Parker, W. C.: Atmospheric wet
776 deposition of mercury and other trace elements in Pensacola, Florida, Atmos. Chem. Phys.,
777 10, 4867-4877, 10.5194/acp-10-4867-2010, 2010.
778 Landis, M. S., Ryan, J. V., Schure, ter, A. F. H. and Laudal, D.: Behavior of Mercury Emissions
779 from a Commercial Coal-Fired Power Plant: The Relationship between Stack Speciation and
780 Near-Field Plume Measurements, Environ. Sci. Technol., 48, 22, 13540–13548,
781 doi:10.1021/es500783t, 2014.
782 Liang, Q., Stolarski, R. S., Kawa, S. R., Nielsen, J. E., Douglass, A. R., Rodriguez, J. M., Blake, D. R.,
783 Atlas, E. L. and Ott, L. E.: Finding the missing stratospheric Br-y: a global modeling study of
784 CHBr3 and CH2Br2, Atmos. Chem. Phys., 10, 5, 2269–2286, 2010.
785 Liang, Q., Atlas, E., Blake, D., Dorf, M., Pfeilsticker, K., and Schauffler, S.: Convective transport of
786 very short lived bromocarbons to the stratosphere, Atmos. Chem. Phys., 14, 5781-5792,
787 doi:10.5194/acp-14-5781-2014, 2014.
788 Lindberg, S. and Stratton, W.: Atmospheric mercury speciation: Concentrations and behavior of
789 reactive gaseous mercury in ambient air, Environ. Sci. Technol., 32, 49-57,
790 10.1021/es970546u, 1998.
791 Lin, J.-T. and McElroy, M. B.: Impacts of boundary layer mixing on pollutant vertical profiles in
792 the lower troposphere: Implications to satellite remote sensing, Atmos. Environ., 44, 14,
793 1726–1739, doi:10.1016/j.atmosenv.2010.02.009, 2010.
794 Liu, G., Cai, Y., Kalla, P., Scheidt, D., Richards, J., Scinto, L. J., Gaiser, E., and Appleby, C.: Mercury
795 mass budget estimates and cycling seasonality in the Florida everglades, Environ. Sci.
796 Technol., 42, 1954-1960, 10.1021/es7022994, 2008.
797 Long, M.S., Keene, W.C., Easter, R.C., Sander, R., Liu, X., Kerkweg, A., and Erickson, D.:
798 Sensitivity of tropospheric chemical composition to halogen-radical chemistry using a fully
799 coupled size-resolved multiphase chemistry-global climate system: halogen distributions,
800 aerosol composition, and sensitivity of climate-relevant gases, 14, 7, 3397-3425, DOI:
801 10.5194/acp-14-3397-2014, 2014.

802 Lyman, S. N., Gustin, M. S., Prestbo, E. M., Kilner, P. I., Edgerton, E. and Hartsell, B.: Testing and
803 Application of Surrogate Surfaces for Understanding Potential Gaseous Oxidized Mercury
804 Dry Deposition, Environ. Sci. Technol., 43, 16, 6235–6241, doi:10.1021/es901192e, 2009.
805 Lyman, S. N. and Jaffe, D. A.: Formation and fate of oxidized mercury in the upper troposphere
806 and lower stratosphere, Nat. Geosci., 5, 114-117, 10.1038/NGEO1353, 2012.
807 Marsh, D., Mills, M. J., Kinnison, D. E., Garcia, R. R., Lamarque, J-F, Calvo, N.: Climate Change
808 from 1850-2005 simulated in CESM1 (WACCM), J. Climate, 26, 19, 7372-7391,
809 doi:10.1175/JCLI-D-12-00558.1, 2013.
810 McClure, C.D., Jaffe, D.A., Edgerton, E.S.: Evaluation of the KCl denuder method for gaseous
811 oxidized mercury using $HgBr_2$ at an in-service AMNet site, Environ. Sci. Technol., 43, 19,
812 11437-11444, doi: 10.1021/es502545k, 2014.
813 McGrath-Spangler, E. L. and Molod, A.: Comparison of GEOS-5 AGCM planetary boundary layer
814 depths computed with various definitions, Atmos. Chem. Phys., 14, 13, 6717–6727,
815 doi:10.5194/acp-14-6717-2014, 2014.
816 Meller, R. and Moortgat, G.: Temperature dependence of the absorption cross sections of
817 formaldehyde between 223 and 323 K in the wavelength range 225-375 nm, J. Geophys.
818 Res. -Atmos., 105, 7089-7101, 10.1029/1999JD901074, 2000.
819 Nair, U. S., Wu, Y., Walters, J., Jansen, J. and Edgerton, E. S.: Diurnal and seasonal variation of
820 mercury species at coastal-suburban, urban, and rural sites in the southeastern United
821 States, Atmos. Environ., 47, 499–508, doi:10.1016/j.atmosenv.2011.09.056, 2012.
822 Nair, U. S., Wu, Y., Holmes, C. D., Ter Schure, A., Kallos, G., and Walters, J. T.: Cloud-resolving
823 simulations of mercury scavenging and deposition in thunderstorms, Atmos. Chem. Phys.,
824 13, 10143-10157, 10.5194/acp-13-10143-2013, 2013.
825 Parrella, J. P., Jacob, D. J., Liang, Q., Zhang, Y., Mickley, L. J., Miller, B., Evans, M. J., Yang, X.,
826 Pyle, J. A., Theys, N., and van Roozendael, M.: Tropospheric bromine chemistry: implications
827 for present and pre-industrial ozone and mercury, Atmos. Chem. Phys., 12, 6723–6740,
828 doi:10.5194/acp-12-6723-2012, 2012.
829 Pehkonen, S.O. and Lin, C.J.: Aqueous photochemistry of mercury with organic acids, J. Air
830 Waste Manage., 48, 2, 144-150, 1998.

831 Prados-Roman, C., Butz, A., Deutschmann, T., Dorf, M., Kritten, L., Minikin, A., Platt, U.,
832 Schlager, H., Sihler, H., Theys, N., van Roozendael, M., Wagner, T. and Pfeilsticker, K.:
833 Airborne DOAS limb measurements of tropospheric trace gas profiles: case studies on the
834 profile retrieval of $O_4$ and BrO, Atmos. Meas. Tech., 4, 1241-1260, doi:10.5194/amt-4-1241-
835 2011, 2011.
836 Pundt, I., Pommereau, J.-P., Chipperfield, M.P., van Roozendael, M. and Goutail, F.: Climatology
837 of the stratospheric BrO vertical distribution by balloon-borne UV-visible spectrometry, J.
838 Geophys. Res. -Atmos., ACH 23-1–ACH 23-14, 107, D24, 10.1029/2002JD002230, 2002.
839 Read, K.A., Mahajan, A.S., Carpenter, L.J., Evans, M.J., Faria, B.V.E., Heard, D.E., Hopkins, J.R.,
840 Lee, J.D., Moller, S.J., Lewis, A.C., Mendes, L., McQuaid, J.B., Oetjen, H., Saiz-Lopez, A.,
841 Pilling, M.J., and Plane, J.M.C.: Extensive halogen-mediated ozone destruction over the
842 tropical Atlantic Ocean, Nature, 453, 7199, 10.1038/nature07035, 1232-1235, 2008.
843 Rienecker, M. M., Suarez, M. J., Gelaro, R., Todling, R., Bacmeister, J., Liu, E., Bosilovich, M. G.,
844 Schubert, S. D., Takacs, L., Kim, G-K, Bloom, S., Chen, J., Collins, D., Conaty, A., da Silva, A.,
845 Gu, W., Joiner, J., Koster, R. D., Lucchesi, R., Molod, A., Owens, T., Pawson, S., Pegion, P.,
846 Redder, C. R., Reichle, R., Robertson, F. R., Ruddick, A. G., Sienkiewicz, M., Woollen, J.:
847 MERRA: NASA's Modern-Era Retrospective Analysis for Research and Applications, J.
848 Climate, 24, 14, 3624-3648, doi:10.1175/JCLI-D-11-00015.1, 2011.
849 Rodgers, C. D.: Inverse Methods for Atmospheric Sounding: Theory and Practice, World
850 Scientific, Singapore, 2000.
851 Rothman, L.S., Jacquemart, D., Barbe, A., Benner, D.C., Birk, M., Brown, L.R., Carleer, M.R.,
852 Chackerian, C., Chance, K., Coudert, L.H., Dana, V., Devi, V.M., Flaud, J.-M., Gamache, R.R.,
853 Goldman, A., Hartmann, J.-M., Jucks, K.W., Maki, A.G., Mandin, J.-Y., Massie, S.T., Orphal, J.,
854 Perrin, A., Rinsland, C.P., Smith, M.A.H., Tennyson, J., Tolchenov, R.N., Toth, R.A., Vander
855 Auwera, J., Varanasi, P., and Wagner, G.: The HITRAN 2004 molecular spectroscopic
856 database, J. Quant. Spectrosc. RA., 96, 139–204, doi: 10.1016/j.jqsrt.2004.10.008, 2005.
857 Rutter, A. P. and Schauer, J. J.: The effect of temperature on the gas-particle partitioning of
858 reactive mercury in atmospheric aerosols, Atmos. Environ., 41, 8647-8657,
859 10.1016/j.atmosenv.2007.07.024, 2007.

860 Saiz-Lopez, A., Lamarque, J.F., Kinnison, D.E., Tilmes, S., Ordonez, C., Orlando, J.J., Conley, A.J.,
861 Plane, J.M.C., Mahajan, A.S., Santos, G.S., Atlas, E.L., Blake, D.R., Sander, S.P., Schauffler, S.,
862 Thompson, A.M., and Brasseur, G.: Estimating the climate significance of halogen-driven
863 ozone loss in the tropical marine troposphere, Atmos. Chem. Phys., 12, 9, 3939-3949,
864 10.5194/acp-12-3939-2012, 2012.
865 Saiz-Lopez, A., Baidar, S., Cuevas, C.A., Koenig, T.K., Fernandez, R.P., Dix, B., Kinnison, D.E.,
866 Lamarque, J.-F., Rodriguez-Lloveras, X., Campos, T. L., and Volkamer, R.: Injection of iodine
867 to the stratosphere, *Geophys. Res. Lett.*, 42, 16, 6852–6859, doi: 10.1002/2015GL064796,
868 2015.
869 Salawitch, R., Weisenstein, D., Kovalenko, L., Sioris, C., Wennberg, P., Chance, K., Ko, M., and
870 McLinden, C.: Sensitivity of ozone to bromine in the lower stratosphere, Geophys. Res. Lett.,
871 32, L05811, 10.1029/2004GL021504, 2005.
872 Sander, R., Keene, W., Pszenny, A., Arimoto, R., Ayers, G., Baboukas, E., Cainey, J., Crutzen, P.,
873 Duce, R., Honninger, G., Huebert, B., Maenhaut, W., Mihalopoulos, N., Turekian, V. and Van
874 Dingenen, R.: Inorganic bromine in the marine boundary layer: a critical review, Atmos.
875 Chem. Phys., 3, D17, 1301–1336, 2003.
876 Schmidt, J. A., D. J. Jacob, H. M. Horowitz, L. Hu, T. Sherwen, M. J. Evans, Q. Liang, R. M.
877 Suleiman, D. E. Oram, M. Le Breton, C. J. Percival, S. Wang, B. Dix, and R. Volkamer:
878 Modeling the observed tropospheric BrO background: Importance of multiphase chemistry
879 and implications for ozone, OH, and mercury, J. Geophys. Res. – Atmos. (in review),
880 submitted 15 Sept 2015.
881 Schofield, R., Johnston, P. V., Thomas, A., Kreher, K., Connor, B.J., Wood, S., Shooter, D.,
882 Chipperfield, M.P., Richter, A., von Glasow, R., and Rodgers, C.D.: Tropospheric and
883 stratospheric BrO columns over Arrival Heights, Antarctica, 2002, J. Geophys. Res-
884 Atmos, 111, D22, D22310, 2006.
885 Schroeder, W. and Munthe, J.: Atmospheric mercury - An overview, Atmos. Environ., 32, 809-
886 822, 10.1016/S1352-2310(97)00293-8, 1998.

887 Selin, N.E., Jacob, D.J., Park, R.J., Yantosca, R.M., Strode, S., Jaegle, L., and Jaffe, D.: Chemical
888 cycling and deposition of atmospheric mercury: Global constraints from observations, J.
889 Geophys. Res., 112, D02308, doi:10.1029/2006JD007450, 2007.
890 Selin, N. E., Jacob, D. J., Yantosca, R. M., Strode, S., Jaeglé, L. and Sunderland, E. M.: Global 3-D
891 land-ocean-atmosphere model for mercury: Present-day versus preindustrial cycles and
892 anthropogenic enrichment factors for deposition, Global Biogeochem Cy, 22, 2, GB2011,
893 doi:10.1029/2007GB003040, 2008.
894 Selin, N. E., Sunderland, E. M., and Knightes, C. D.: Sources of Mercury Exposure for U.S.
895 Seafood Consumers: Implications for Policy, Environ. Health Perspect., 118, 137-143,
896 10.1289/ehp.0900811, 2010.
897 Shah, V., Jaeglé, L., Gratz, L. E., Ambrose, J. L., Jaffe, D. A., Selin, N. E., Song, S., Campos, T. L.,
898 Flocke, F. M., Reeves, M., Stechman, D., Stell, M., Festa, J., Stutz, J., Weinheimer, A. J.,
899 Knapp, D. J., Montzka, D. D., Tyndall, G. S., Apel, E. C., Hornbrook, R. S., Hills, A. J., Riemer,
900 D. D., Blake, N. J., Cantrell, C. A., and Mauldin III, R. L.: Origin of oxidized mercury in the
901 summertime free troposphere over the southeastern US, Atmos. Chem. Phys., 16, 1511-
902 1530, doi:10.5194/acp-16-1511-2016, 2016.
903 Shepler, B., Balabanov, N., and Peterson, K.: Ab initio thermochemistry involving heavy atoms:
904 An investigation of the reactions Hg+IX (X=1, Br, Cl, O), J. Phys. Chem. A, 109, 10363-
905 10372, 10.1021/jp0541617, 2005.
906 Sihler, H., Platt, U., Beirle, S., Marbach, T., Kühl, S., Dörner, S., Verschaeve, J., Frieß, U.,
907 Pöhler, D., Vogel, L., Sander, R., and Wagner, T.: Tropospheric BrO column densities in the
908 Arctic derived from satellite: retrieval and comparison to ground-based measurements,
909 Atmos. Meas. Tech., 5, 2779-2807, doi:10.5194/amt-5-2779-2012, 2012.
910 Spietz, P., Martin, J.C.G., and Burrows, J.P: Spectroscopic studies of the I2/O3 photochemistry –
911 Part 2. Improved spectra of iodine oxides and analysis of the IO absorption spectrum, J.
912 Photoch. Photobio. A., 50-67, 176, 1-3, doi:10.1016/j.jphotochem.2005.08.023, 2005.
913 Soerensen, A. L., Sunderland, E. M., Holmes, C. D., Jacob, D. J., Yantosca, R. M., Skov, H.,
914 Christensen, J. H., Strode, S. A. and Mason, R. P.: An Improved Global Model for Air-Sea

915 Exchange of Mercury: High Concentrations over the North Atlantic, Environ. Sci. Technol.,
916 44, 22, 8574–8580, doi:10.1021/es102032g, 2010.
917 Streets, D., Zhang, Q. and Wu, Y.: Projections of global mercury emissions in 2050, Environ. Sci.
918 Technol., 43, 8, 2983–2988, doi:10.1021/es802474j, 2009.
919 Swartzendruber, P. C., Jaffe, D. A., Prestbo, E. M., Weiss-Penzias, P., Selin, N. E., Park, R., Jacob,
920 D. J., Strode, S., and Jaegle´, L.: Observations of reactive gaseous mercury in the free
921 troposphere at the Mount Bachelor Observatory, J. Geophys. Res., 111, D24301,
922 10.1029/2006JD007415, 2006.
923 Swartzendruber, P. C., Jaffe, D. A., and Finley, B.: Development and first results of an aircraft-
924 based, high time resolution technique for gaseous elemental and reactive (oxidized)
925 gaseous mercury, Environ. Sci. Technol., 43, 7484-7489, 2009.
926 Thalman, R. and Volkamer, R.: Temperature dependent absorption cross-sections of $O_2$-$O_2$
927 collision pairs between 340 and 630 nm and at atmospherically relevant pressure, Phys.
928 Chem. Chem. Phys., 15, 15371-15381, 10.1039/c3cp50968k, 2013.
929 Theys, N., van Roozendael, M., Hendrick, F., Fayt, C., Hermans, C., Baray, J. -., Goutail, F.,
930 Pommereau, J. -., and De Maziere, M.: Retrieval of stratospheric and tropospheric BrO
931 columns from multi-axis DOAS measurements at Reunion Island (21 degrees S, 56 degrees
932 E), Atmos. Chem. Phys., 7, 4733-4749, 2007.
933 Theys, N., van Roozendael, M., Hendrick, F., Yang, X., De Smedt, I., Richter, A., Begoin, M.,
934 Errera, Q., Johnston, P. V., Kreher, K., and De Maziere, M.: Global observations of
935 tropospheric BrO columns using GOME-2 satellite data, Atmos. Chem. Phys., 11, 1791-1811,
936 10.5194/acp-11-1791-2011, 2011.
937 Tong, Y., Eichhorst, T., Olson, M.R., McGinnis, J.E., Turner, I., Rutter, A.P., Shafer, M.M., Wang,
938 X., Schauer, J.J.: Atmospheric photolytic reduction of Hg(II) in dry aerosols, Environ. Sci.
939 Process. Impacts, 15, 10, 1883-1888, doi: 10.1039/c3em00249g, 2013.
940 Tossell, J. A.: Calculation of the energetics for oxidation of gas-phase elemental Hg by Br and
941 BrO, J. Phys. Chem. A, 107, 7804-7808, doi: 10.1021/jp030390m, 2003.
942 Van Roozendael, M., Wagner, T., Richter, A., Pundt, I., Arlander, D., Burrows, J., Chipperfield,
943 M., Fayt, C., Johnston, P., Lambert, J., Kreher, K., Pfeilsticker, K., Platt, U., Pommereau, J.,

Sinnhuber, B., Tornkvist, K., and Wittrock, F.: Intercomparison of BrO measurements from ERS-2 GOME, ground-based and balloon platforms, Remote Sensing of Trace Constituents in the Lower Stratosphere, Troposphere and the Earth's Surface: Global Observations, Air Pollution and the Atmospheric Correction, 29, 1661-1666, 10.1016/S0273-1177(02)00098-4, 2002.

Vandaele, A. C., Hermans, C., Simon, P. C., Carleer, M., Colin, R., Fally, S., Mérienne, M. F., Jenouvrier, A., and Coquart, B.: Measurements of the NO2 absorption cross-section from 42 000 cm−1 to 10 000 cm−1 (238–1000 nm) at 220 K and 294 K, J. Quant. Spectrosc. Ra., 59, 171-184, http://dx.doi.org/10.1016/S0022-4073(97)00168-4, 1998.

Volkamer, R., Spietz, P., Burrows, J., and Platt, U.: High-resolution absorption cross-section of glyoxal in the UV-vis and IR spectral ranges, J. Photoch. Photobio. A., 172, 35-46, 10.1016/j.jphotochem.2004.11.011, 2005.

Volkamer, R., Baidar, S., Campos, T. L., Coburn, S., DiGangi, J. P., Dix, B., Eloranta, E., Koenig, T. K., Morley, B., Ortega, I., Pierce, B. R., Reeves, M., Sinreich, R., Wang, S., Zondlo, M. A., and Romashkin, P. A.: Aircraft measurements of BrO, IO, glyoxal, $NO_2$, $H_2O$, $O_2$-$O_2$ and aerosol extinction profiles in the tropics: Comparison with aircraft-/ship-based in situ and lidar measurements, Atmos. Meas. Tech. 8, 2121-2148, 2015. doi:10.5194/amt-8-2121-2015.

Wang, S., Schmidt, J.A., Baidar, S., Coburn, S., Dix, B., Koenig, T., Apel, E.C., Bowdalo, D., Campos, T.L., Eloranta, E., Evans, M.J., diGangi, J.P., Zondlo, M.A., Gao, R.S., Haggerty, J.A., Hall, S.R., Hornbrook, R.S., Jacob, D.J., Morley, B., Pierce, B.R., Reeves, M., Romashkin, P.A., ter Schure, A., and Volkamer, R.: Active and widespread halogen chemistry in the tropical and subtropical free troposphere, P. Natl. Acad. Sci. USA, 2015.

Weiss-Penzias, P., H. M. Amos, N. E. Selin, M. S. Gustin, D. A. Jaffe, D. Obrist, G. R. Sheu, and A. Giang: Use of a global model to understand speciated atmospheric mercury observations at five high-elevation sites, Atmos. Chem. Phys., 15, 3, 1161–1173, doi:10.5194/acp-15-1161-2015, 2015.

971 Weiss-Penzias, P. S., Gustin, M. S. and Lyman, S. N.: Source of gaseous oxidized mercury and
972 mercury dry deposition at two southeastern U.S. sites, Atmos. Environ., 45, 27, 4569–4579,
973 doi:10.1016/j.atmosenv.2011.05.069, 2011.
974 Wilmouth, D., Hanisco, T., Donahue, N., and Anderson, J.: Fourier transform ultraviolet
975 spectroscopy of the A 2Π3/2 <- X 2Π3/2 transition of BrO, J. Phys. Chem. A, 103, 8935-
976 8945, 10.1021/jp991651o, 1999.
977 Yang, X., Cox, R.A., Warwick, N.J., Pyle, J.A., Carver, G.D., O'Connor, F.M., and Savage, N.H.:
978 Tropospheric bromine chemistry and its impacts on ozone: A model study, D23311, J.
979 Geophys. Res. -Atmos., 110, D23, 10.1029/2005JD006244, 2005.
980 Zhang, Y., Jaegle, L., van Donkelaar, A., Martin, R. V., Holmes, C. D., Amos, H. M., Wang, Q.,
981 Talbot, R., Artz, R., Brooks, S., Luke, W., Holsen, T. M., Felton, D., Miller, E. K., Perry, K. D.,
982 Schmeltz, D., Steffen, A., Tordon, R., Weiss-Penzias, P. and Zsolway, R.: Nested-grid
983 simulation of mercury over North America, Atmos. Chem. Phys., 12, 14, 6095–6111, 2012.
984

985 **Supplement**

986 **S1 Instrument and Measurement Site**

987 The instrument and measurement site are identical to that described in Coburn et al. (2011).
988 Only a brief overview will be given here. For the duration of the measurements discussed in this
989 study, a research-grade MAX-DOAS instrument was located at a United States Environmental
990 Protection Agency (US EPA) facility in Gulf Breeze, FL (30.3N 87.2W) and measured for time
991 periods between May 2009 and February 2011. This site is ~10 km southeast of Pensacola, FL
992 (population appr. 50,000) and ~1 km from the coast of the Gulf of Mexico, which enables the
993 measurement of urban and marine air masses. The spectrometer and controlling electronics
994 were set-up in the warehouse of the EPA facility, while the telescope was mounted on a
995 support structure on the roof of the warehouse (~10-12 m above sea level) connected via an
996 optical fiber. The telescope was oriented ~40° west of true north in order to realize a clear view
997 in the lowest elevation angles to the coast. During operation the full 180° elevation angle range
998 of the telescope was utilized to enable the characterization of air-masses over the seawater
999 lagoon to the North, and over the coastal region of the Gulf of Mexico to the South. For the
1000 purposes of this study, the north viewing direction will be considered to minimize changes in
1001 the radiative transfer calculations due to azimuth effects throughout the day.
1002 The instrument used for this study consists of a Princeton Instruments Acton SP2300i Czerny-
1003 Turner grating (500 groove/mm with a 300nm blaze angle) spectrometer with a PIXIS 400B
1004 back-illuminated CCD detector (Coburn et al., 2011). This setup was optimized to cover the
1005 wavelength range ~321-488 nm with an optical resolution of ~0.68 nm full-width at half the
1006 maximum (FWHM). The spectrometer is coupled to a weather-resistant telescope (capable of
1007 rotating the elevation angle by 180°, 50 mm f/4 optics) via a 10 m long 1.7 mm diameter quartz
1008 fiber. During normal field operation this instrument was routinely able to realize values of the
1009 root mean square (RMS) of the residual remaining after the DOAS fitting procedure on the
1010 order 0.9-3x$10^{-4}$. This system was very stable, with little need for maintenance, and was
1011 operated remotely for periods between May 2009 and February 2011 to measure multiple
1012 trace gases, including: BrO, IO, nitrogen dioxide ($NO_2$), formaldehyde (HCHO), glyoxal
1013 (CHOCHO), and the oxygen molecule collision induced absorption signal (referred to as $O_4$).

## S2 DOAS retrieval sensitivity studies

**S2.1 Retrieval window:** Several sensitivity studies were performed to determine the most suitable analysis settings for the BrO retrieval. This was accomplished through a comparison of both $O_3$ and HCHO dSCD values from the BrO fitting window with dSCDs predicted using WACCM vertical profiles. Also, the effect of using different $O_4$ reference cross-sections was tested with respect to the $O_4$ dSCD in the BrO fitting window.

WACCM model output profiles for $O_3$ and HCHO were used to forward calculate dSCDs for comparison to measured dSCDs of $O_3$ and HCHO retrieved using the BrO fitting window. Five different BrO analysis setting windows were tested: 1) fitting window 345-359nm with a $2^{nd}$ order polynomial (encompasses two BrO absorption peaks – 2-band analysis); 2) fitting window 346-359nm with a $2^{nd}$ order polynomial (2-band analysis); 3) fitting window 340-359nm with a $3^{rd}$ order polynomial (3-band analysis); 4) fitting window 340-359nm with a $5^{th}$ order polynomial (3-band analysis); and 5) fitting window 338-359nm with a $5^{th}$ order polynomial (4-band analysis). It was determined that analysis setting 5) (4-band analysis with $5^{th}$ order polynomial) including a constrained intensity offset (Sect. S2.2) best represented both $O_3$ and HCHO. These are the analysis settings that were then used to assess the effects of different $O_4$ cross sections in the BrO fitting window: 1) Hermans (2002); 2) Greenblatt et al. (1990); and 3) Thalman and Volkamer (2013). The $O_4$ dSCDs retrieved from the BrO fitting window were compared with the $O_4$ dSCDs retrieved from an $O_4$ optimized fitting window in the UV (353-387 nm); and while none of the cross sections are able to fully reproduce the $O_4$ dSCDs from the $O_4$ optimized window, the Thalman and Volkamer (2013) cross-section was deemed to be an improvement over Hermans and Greenblatt/Burkholder in representing $O_4$ in the BrO fitting window.

**S2.2 Intensity offset:** An additional parameter that can be utilized in the DOAS retrieval is an intensity offset, which would be used to help account for any instrument stray light. The instrument employed for this study was designed to actively minimize spectrometer stray light through the use of cut-off filters (BG3 and BG38), as well as the method of background correction. The background correction is similar to that described in Wagner et al. (2004) and utilizes dark regions on the CCD detector to correct for dark current and offset noise as well as

stray light. It was determined that stray light in the instrument was only a few percent (before correction) in the wavelength range 330-360 nm. Fitting an intensity offset should only account for uncorrected stray light and is expected to be on the order of magnitude of the error in the background correction. The fitting of this parameter typically helps reduce the RMS of the fitting routine, thus improving instrument sensitivity. However, preliminary studies found a significant effect on the retrieved BrO dSCDs depending on whether or not this parameter was included in the fitting routine, and that this effect was most pronounced in the narrower fitting windows. In the most extreme case (analysis window 346-359 nm), retrieved BrO dSCDs changed from ~$1x10^{14}$ molec $cm^{-2}$ without fitting the intensity offset to values less than zero when an unconstrained intensity offset was included. In all fitting windows tested, utilizing an unconstrained intensity offset resulted in the highest fit factor for the offset and lowest values for the BrO dSCDs, and in some cases lead to significantly negative (non-physical) values. In these cases, it was found that periods of time existed when the fit factor for the intensity offset was much greater than what was determined to be a reasonable value for this instrument. For this reason, the intensity offset was kept in the retrieval (to help with RMS), but limited to a range determined by the upper limit of this estimated correction ($\pm 3x10^{-3}$).

Based on the findings of the offset sensitivity tests and the dSCD comparison tests presented in this section, the dSCDs used for the BrO inversion are from the 338-359 nm fitting window utilizing a $5^{th}$ order polynomial, the constrained intensity offset, and the Thalman and Volkamer (2013) $O_4$ cross-section.

## S3 Aerosol Retrieval

Aerosol profiles are determined through an iterative comparison of measured $O_4$ dSCDs (analyzed in the wavelength window 437-486 nm) with $O_4$ dSCDs calculated from the RTM McArtim3 (Deutschmann et al., 2011) outputs based on specific aerosol extinction profiles. This process is performed on each set of MAX-DOAS viewing angles (for this point forward referred to as a scan) of the case study day (total of 56 scans) in order to determine individual aerosol profiles. The initial aerosol profile used for each scan decreased exponentially with altitude from a value of 0.01 $km^{-1}$ at 483 nm (scale height of 0.6 km). This wavelength is chosen for its proximity to the $O_4$ peak absorption structure at 477 nm while avoiding the feature itself, as

well as avoiding absorption structures from other trace gases (i.e. $NO_2$). This $O_4$ fitting window was chosen due to the better general agreement achieved between measured and forward calculated $O_4$ dSCDs (calculated after aerosol extinction profiles were determined) as compared with the $O_4$ retrieval in the UV range. This is similar to findings from Volkamer et al., (2015), where it is determined that using the 477 nm $O_4$ band for deriving aerosol profiles is much more robust than using the UV bands due to the increased Rayleigh scattering at shorter wavelengths, which can mask aerosol extinction.

The $O_4$ vertical profiles used for all calculations and as input to the RTM are based on temperature and pressure profiles available from NOAA's ESRL Radiosonde Database for locations close to the measurement site, which are in good agreement with the corresponding profiles from WACCM. In each step of the iteration the measured $O_4$ dSCDs are compared to the forward calculated dSCDs at each elevation angle of the scan being analyzed, and the differences between these values are used as input for optimizing the modification of the aerosol profile for the subsequent iteration. For this study, the convergence limit is set at a percent difference of 5% between the lowest two elevation angle dSCDs, or if the process reaches 5 iterations without finding convergence the last aerosol profile is used. The limit of 5 iterations is chosen as a compromise between achieving optimal agreement between the $O_4$ dSCDs and data computation time. For this case study, the 5% criterion is reached for every sequence. The resulting time series of aerosol extinction profiles are shown in Fig. S10 (Supplement).

The aerosol extinction profiles at 483 nm were scaled to derive extinction at 350 nm using the relationship found in Eq. (S1).

$$\varepsilon_{350} = \varepsilon_{483} \cdot \left(\frac{350}{483}\right)^{-1.25} \quad \text{(S1)}$$

where $\varepsilon_{350}$ and $\varepsilon_{483}$ represent aerosol extinction coefficients at 350 and 483 nm, respectively. An Angstrom exponent of -1.25 was chosen as a moderate value that would be representative of an average atmosphere (Dubovik et al., 2002). The retrieved aerosol profiles at 350 nm provided input to the RTM in order to calculate the appropriate weighting functions for BrO.

## S4 Box Model Description

The modeling portion of this study is designed to assess the concentration of Br radicals available to participate in the mercury oxidation reaction based on BrO vertical profiles provided from the MAX-DOAS measurements and GEOS-Chem. Other trace gas and atmospheric parameter inputs to the diurnal steady-state box model (Dix et al., 2013, Wang et al., 2015) are median daily profiles derived from the MAX-DOAS measurements, WACCM, and GEOS-Chem. A single median profile representing the entire day (daily median, for each model input) is used rather than individual profiles. From these profiles, the box model then calculates the partitioning between bromine species throughout the troposphere (including: reactions with other trace gases; photolysis; and some aqueous phase partitioning and chemistry) in order to derive vertical profiles of the Br radical, which are subsequently used for calculating mercury oxidation rates. A summary of all the reactions involving mercury compounds considered in the box model along with associated rate coefficients can be found in Table 2. The model conceptually follows the framework of Crawford et al., (1999), where model inputs are initiated and allowed to reach steady-state over several days. In the box model, the BrO and IO (to assess the impact of iodine radical species in the mercury oxidation reactions) profiles are taken from the MAX-DOAS measurements; however, the GEOS-Chem BrO profile is also used in order to assess the impact of the differences between these profiles. Other box model inputs are taken as the output profiles from the external models utilized in this study and these include: temperature, pressure, and HCHO from WACCM; and $O_3$ and $NO_2$ from GEOS-Chem. As a sensitivity test WACCM $O_3$ and $NO_2$ were also used to assess the impact on the mercury oxidation scheme towards differences in the vertical distributions of these molecules. The resulting vertical profiles of the rate of mercury oxidation using these two profiles as box model inputs is found in Fig. S11 (Supplement), which follows the same format as Fig. 7. Aerosol surface area measurements from the TORERO data set (Volkamer et al., 2015; Wang et al., 2015) are assumed representative of conditions in the marine atmosphere, and therefore used as model inputs for lack of independent measurements. The vertical distribution of $Hg^0$ from GEOS-Chem was used in all scenarios. Additionally, photolysis rates for a variety of species, calculated using the Tropospheric Ultraviolet and Visible (TUV) Radiation model, are included. The TUV model was initiated for a Rayleigh atmosphere (aerosol extinction = 0), with $O_3$ and

$NO_2$ columns of 380 and 0.3 Dobson Units (DU), respectively, which are derived from the average vertical profiles from WACCM. Since the median BrO profile derived by the MAX-DOAS measurements closely resembles the profiles retrieved around solar noon (see Fig. 5), the TUV calculations from this time are used. For the model runs comparing the BrO profiles from the measurements and GEOS-Chem, only the BrO profile is changed; all other inputs remain constant.

For the determination of the dominant oxidative pathways, the reaction rates for oxidation of $Hg^0$ against Br and $O_3$ are calculated as a function of altitude for the different reactant vertical profiles, which is important due to atmospheric temperature gradients. This also allows the assessment of the relative contributions of these reactions to the overall rate of oxidation as a function of altitude. Oxidation by $O_3$ is included in the box model due to the amount of evidence from laboratory studies indicating that this reaction might play a role in the atmosphere; although potentially not completely in the gas phase.

Following Wang et al. (2015), the box model is initiated under two different modes to investigate the sensitivity of oxidation rates, and likely product distributions to the mechanistic assumptions about mercury oxidation. The two modes differ in the scavenging reactions of the HgBr adduct. A “traditional” scenario only includes Br and OH radicals as scavengers (Holmes et al., 2009), and a “revised” mode includes species suggested by Dibble et al., 2012 (BrO, NO2, and HO2) as well as additional halogen species (I and IO). The model also tracks the concentrations of all species as a function of altitude, which gives indications for the product distributions of the various reactions.

**References (Supplement)**

Coburn, S., Dix, B., Sinreich, R., and Volkamer, R.: The CU ground MAX-DOAS instrument: characterization of RMS noise limitations and first measurements near Pensacola, FL of BrO, IO, and CHOCHO, Atmos. Meas. Tech., 4, 2421-2439, 10.5194/amt-4-2421-2011, 2011.

Crawford, J., Davis, D., Olson, J., Chen, G., Liu, S., Gregory, G., Barrick, J., Sachse, G., Sandholm, S., Heikes, B., Singh, H., and Blake, D.: Assessment of upper tropospheric HOx sources over the tropical Pacific based on NASA GTE/PEM data: Net effect on HOx and other

photochemical parameters, J. Geophys. Res. -Atmos., 104, 16255-16273, 10.1029/1999JD900106, 1999.

Deutschmann, T., Beirle, S., Friess, U., Grzegorski, M., Kern, C., Kritten, L., Platt, U., Prados-Roman, C., Pukite, J., Wagner, T., Werner, B., and Pfeilsticker, K.: The Monte Carlo atmospheric radiative transfer model McArtim: Introduction and validation of Jacobians and 3D features, J. Quant. Spectrosc. Radiat. Transfer, 112, 1119-1137, 10.1016/j.jqsrt.2010.12.009, 2011.

Dibble, T. S., Zelie, M. J., and Mao, H.: Thermodynamics of reactions of ClHg and BrHg radicals with atmospherically abundant free radicals, Atmos. Chem. Phys., 12, 10271-10279, 10.5194/acp-12-10271-2012, 2012.

Dix, B., Baidar, S., Bresch, J. F., Hall, S. R., Schmidt, K. S., Wang, S., and Volkamer, R.: Detection of iodine monoxide in the tropical free troposphere, Proc. Natl. Acad. Sci. U. S. A., 110, 2035-2040, 10.1073/pnas.1212386110, 2013.

Dubovik, O., Holben, B., Eck, T.F., Smirnov, A., Kaufman, Y.J., King, M.D., Tanre, D., Slutsker, I.: Variability of absorption and optical properties of kef aerosol types observed in worldwide locations, J. Atmos. Sci., 59, 3, 590-608, doi: 10.1175/1520-0469(2002)059<0590:VOAAOP>2.0.CO;2, 2002.

Greenblatt, G., Orlando, J., Burkholder, J. and Ravishankara, A.: Absorption-Measurements of Oxygen between 330nm and 1140nm, J. Geophys. Res. -Atmos., 95, 18577-18582, 10.1029/JD095iD11p18577, 1990.

Hermans, C., Measurement of absorption cross sections and spectroscopic molecular parameters: O2 and its collisional induced absorption: http://www.aeronomie.be/spectrolab/o2, 2002.

Wagner, T., Dix, B., von Friedeburg, C., Frieß, U., Sanghavi,S., Sinreich, R., and Platt, U.: MAX-DOAS O4 measurements: A new technique to derive information on atmospheric aerosols. Principles and information content, J. Geophys. Res. 109, D22205, doi:10.1029/2004JD004904, 2004.al. (2004)

Holmes, C. D., Jacob, D. J., Mason, R. P., and Jaffe, D. A.: Sources and deposition of reactive gaseous mercury in the marine atmosphere, Atmos. Environ., 43, 2278-2285, 10.1016/j.atmosenv.2009.01.051, 2009.

Thalman, R. and Volkamer, R.: Temperature dependent absorption cross-sections of $O_2$-$O_2$ collision pairs between 340 and 630 nm and at atmospherically relevant pressure, Phys. Chem. Chem. Phys., 15, 15371-15381, 10.1039/c3cp50968k, 2013.

Volkamer, R., Baidar, S., Campos, T. L., Coburn, S., DiGangi, J. P., Dix, B., Eloranta, E., Koenig, T. K., Morley, B., Ortega, I., Pierce, B. R., Reeves, M., Sinreich, R., Wang, S., Zondlo, M. A., and Romashkin, P. A.: Aircraft measurements of BrO, IO, glyoxal, $NO_2$, $H_2O$, $O_2$-$O_2$ and aerosol extinction profiles in the tropics: Comparison with aircraft-/ship-based in situ and lidar measurements, Atmos. Meas. Tech. 8, 2121-2148, 2015. doi:10.5194/amt-8-2121-2015.

Wang, S., Schmidt, J.A., Baidar, S., Coburn, S., Dix, B., Koenig, T., Apel, E.C., Bowdalo, D., Campos, T.L., Eloranta, E., Evans, M.J., diGangi, J.P., Zondlo, M.A., Gao, R.S., Haggerty, J.A., Hall, S.R., Hornbrook, R.S., Jacob, D.J., Morley, B., Pierce, B.R., Reeves, M., Romashkin, P.A., ter Schure, A., and Volkamer, R.: Active and widespread halogen chemistry in the tropical and subtropical free troposphere, P. Natl. Acad. Sci. USA, 2015.

1202

1203 **Table 1**: Overview of DOAS settings

| Cross Section, Parameter | Reference | BrO window (338-359 nm) | IO window (415-438 nm) | $NO_2$ window (434-460 nm) | $O_4$ window (437-486 nm) |
|---|---|---|---|---|---|
| Polynomial Order | | 5 | 5 | 3 | 5 |
| $O_3$ T = 223 K | Bogumil et al. (2003) | X | X | X | X |
| $O_3$ T = 243 K | Bogumil et al. (2003) | X | X | X | X |
| $NO_2$ T = 220 K | Vandaele et al. (1997) | X | X | X | X |
| $NO_2$ T = 220 K | Vandaele et al. (1997) | X | X | X | X |
| $O_4$ T = 293 | Thalman and Volkamer (2013) | X | | X | X |
| BrO | Wilmouth et al. (1999) | X | | | |
| HCHO | Meller and Moortgat (2000) | X | | | |
| IO | Spietz et al. (2005) | | X | | |
| CHOCHO | Volkamer et al. (2005 | | | X | |
| $H_2O$ | Rothman et al. (2005) | | | X | X |

1204

**Table 2**: Summary of mercury reactions and rate coefficients used in box-model

| Reaction | Rate or equilibrium[1] Coefficient[2] | Reference |
|---|---|---|
| $Hg^0 + O_3 \rightarrow HgO + O_2$ | $3x10^{-20}$ | Hall (1995) |
| $HgO_{(g)} \leftrightarrow HgO_{(aq)}$ | $K_{eq}$[1] | Rutter and Schauer (2007) |
| $HgO_{(aq)} \rightarrow Hg^0_{(g)}$ | $1.12x10^{-5}$ | Costa and Liss (1999) |
| $HgClY_{(g)} \leftrightarrow HgClY_{(aq)}$ | $K_{eq}$[1] | Rutter and Schauer (2007) |
| $HgClY_{(aq)} \rightarrow Hg^0_{(g)}$ | $1.12x10^{-5}$ | Costa and Liss (1999) |
| $Hg^0 + Br \xrightarrow{M} HgBr$ | $1.46x10^{-32}*(\frac{T}{298})^{-1.86}*[M]$ | Donohoue (2006) |
| $HgBr + M \rightarrow Hg^0 + Br + M$ | $4.0x10^{9}*\exp(\frac{-7292}{T})$ | Goodsite et al., (2012) |
| $HgBr_{(g)} \leftrightarrow HgBr_{(aq)}$ | $K_{eq}$[1] | Rutter and Schauer (2007) |
| $HgBr + Y$[4] $\rightarrow HgBrY$ | $2.5x10^{-10}*(\frac{T}{298})^{-0.57}$ | Goodsite et al. (2004) |
| $\rightarrow Hg^0 + Br_2$ | $3.9x10^{-11}$ | Balabanov et al., (2005) |
| $HgBrY_{(g)} \leftrightarrow HgBrY_{(aq)}$ | $K_{eq}$[1] | Rutter and Schauer (2007) |
| $HgBrY_{(aq)} \rightarrow Hg^0_{(g)}$ | $1.12x10^{-5}$ | Costa and Liss (1999) |
| $HgBr + Y'$[5] $\rightarrow HgBr\ Y'$ | $1x10^{-10}$ | Dibble et al. (2012) |
| $HgBrY'_{(g)} \leftrightarrow HgBrY'_{(aq)}$ | $K_{eq}$[1] | Rutter and Schauer (2007) |
| $HgBrY'_{(aq)} \rightarrow Hg^0_{(g)}$ | $1.12x10^{-5}$ | Costa and Liss (1999) |

[1]Equilibrium coefficient is parameterized according to Rutter and Schauer (2007): Keq = (SA-PM)/$10^{((-4250/T)+10)}$, where SA = the specific aerosol surface area, and PM = the particulate mass

[2]Rate coefficients are given in either $cm^3\ molec^{-1}\ s^{-1}$ or $s^{-1}$

[3]Assumes that the reaction between $Hg^0$ and Cl is the rate limiting step to form HgCl which will then quickly react with Br to form HgClBr

[4]Y = Br, OH

[5]Y' = $HO_2$, $NO_2$, BrO, IO, I

**Figure Captions**

**Figure 1**: Total mercury wet deposition in the US for 2013. The highest levels of Hg deposition are observed in the southeastern US, where no local and regional sources are located immediately upwind. The black square indicates the measurement location.

**Figure 2**: Overview of the MAX-DOAS measurements for the week surrounding the case study day (9 April, highlighted with blue box). Also included are $O_3$ measurements from a monitor collocated with the MAX-DOAS instrument (label "CU", black trace) and a monitor located at an Mercury Deposition Network (MDN) site ~30 km northwest of the EPA site (label "OLF", red trace), and wind direction measurements (grey trace) from a site near the EPA facility along with $Hg^{II}$ measurements from the MDN site (scaled by a factor of 10, orange trace).

**Figure 3**: Conceptual sketch of the $SCD_{Ref}$ retrieval (panel a), and resulting $SCD_{Ref}$ values (black trace). The sensitivity of the a-posteriori BrO VCD (red trace) to $SCD_{Ref}$ is also shown (panel b).

**Figure 4:** Characterizing the retrieval averaging kernel (AVK) and Degrees of Freedom (DoF). Panel a) AVK output for an inversion of BrO SCDs (at SZA = 25°) as a function of altitude. The colored traces represent the individual altitude grids of the inversion accounting for $SCD_{Ref}$; the thick black trace is the diagonal of the AVK matrix; the thick red trace is the diagonal of the AVK matrix from the inversion not accounting for $SCD_{Ref}$. Panel b) shows the difference between the two AVK diagonals as a function of altitude.

**Figure 5**: BrO profiles for a single MAX-DOAS measurement scan at SZA ~23° around solar noon. Panel a) contains three of the a-priori profiles tested (dashed lines) and the respective a-posteriori profiles (solid lines); colors correspond to use of WACCM (black); GEOS-CCM (orange); and TORERO RF12 (blue) as a-priori information. Panel b) contains the AVK from the inversion using the WACCM profile as the a-priori, and gives an indication on the amount of information coming from the measurements as a function of altitude.

**Figure 6**: Diurnal variation in the BrO vertical profiles represented as partial VCDs for the BL (0-1 km), troposphere (0-15 km), total (0-50 km) (panel b), and the total DoFs from the inversion for each profile in panel a. The error bars on the VCDs indicate the range of values retrieved using the three different a-priori profiles.

**Figure 7**: Box model results of the rate of mercury oxidation as a function of altitude for two species: 1) 2) ozone (red); and 3) bromine radicals (solid blue: MAX-DOAS; dashed pink: GEOS-Chem) (panel a); the corresponding lifetimes are found in panel b. The black dashed line at 4 km shows where measurement sensitivity starts to drop because of the decreasing amount of BrO (the measured parameter) in the lower layers of the atmosphere.

**Figure 8**: Box model results for the scavenging of the HgBr adduct as a function altitude for two different reaction schemes: traditional (panel a) and revised (panel b). Panel c contains the ratio of the total rates (black traces in panels a) and b) to show the enhancement in the rate of the scavenging reaction when other reactants are taken into consideration.

**Figure 9:** Observed (black solid trace) and simulated (blue traces) concentrations of oxidized mercury ($Hg^{II}$ = GOM + PBM) during April 2010 (9 April highlighted). Model results from GEOS-Chem (solid) include a sensitivity test, labeled FT (dashed trace), in which North American anthropogenic emissions are zero and no GEM oxidation occurs in the lower troposphere (>700 hPa); therefore all $Hg^{II}$ in the "FT" model is derived from oxidation of in the free troposphere or long-range transport.

**Figure S1**: BrO box-AMFs for two elevation angles (25° and 90°, solid and dashed lines respectively) at different SZAs. For these higher pointing elevation angles, the box-AMFs peak at altitudes of 2-15km (free troposphere) for SZAs lower than 70°, while at higher SZA the box-AMFs indicate that the sensitivity towards the free troposphere is decreasing.

**Figure S2**: Overview of box-AMFS for SZAs less than 70° for 4 elevation angles: a) 3.8°; b) 10°; c) 25°; and d) 90°.

**Figure S3**: Overview of the WACCM BrO vertical profiles as a function of altitude and time of day (panel a), and then collapsed into to the corresponding partial (green trace) and total (blue trace) VCDs in panel b.

**Figure S4**: Example results for the inversion of IO from the MAX-DOAS measurements. Panel a) contains the three a-priori profiles used in the inversion (dashed, colored lines), the a-posteriori results from a MAX-DOAS scan at ~45° SZA (morning) corresponding to the a-priori profiles (solid lines, colors correspond with the a-priori), and the median IO profile (red trace, where the error bars reflect the $25^{th}$ and $75^{th}$ percentiles). Panel b) shows the averaging kernels for the

inversion using a-priori "Prf1". Panel c) shows the diurnal variation of the IO VCD for the BL (0-1 km), troposphere (0-15 km), and total (0-25 km).

**Figure S5:** Overview of the sensitivity of $SCD_{Ref}$ and the derived VCDs on the choice of reference spectra/scan and a-priori profile assumption. Panel (a) contains the $SCD_{Ref}$ determined from both forward calculations of the a-priori profiles (grey traces) and the iterative approach (blue traces) for 47 different zenith spectra. The a-priori cases corresponding to the median BrO profile based on WACCM (WACCM*1.4) are denoted with thicker and darker lines. The error bars on the forward calculated median BrO profile case (dark grey) reflect the $\pm 1 \times 10^{13}$ molec $cm^{-2}$ criteria for selecting suitable references. Panel (b) contains the corresponding VCDs derived for one MAX-DOAS scan (near solar noon) for each of the references and a-priori combinations. The blue shaded vertical boxes denote references that meet the criteria for being used in the inversion; and the horizontal grey box (panel b) covers the range of $2.3 \pm 0.9 \times 10^{13}$ molec $cm^{-2}$, which fully captures all the references contained within the shaded blue region.

**Figure S6:** Time series of the DoFs and inversion RMS for three different analysis procedures: 1) changing reference analysis (reference is selected from each measurement scan throughout the day, blue trace); 2) fixed reference without accounting for any $SCD_{Ref}$ (green trace); and 3) fixed reference analysis accounting for $SCD_{Ref}$ (red trace). Included in the plot is SZA (black trace) for reference.

**Figure S7**: Shows a comparison of the measured BrO dSCDs and the dSCDs calculated from the a-posteriori profiles (inversion using the WACCM profile) for both the entire case study day (panel a) and for a small subset of scans before solar noon (panel b). Panel c contains the RMS of the difference between the measured and calculated dSCDs for each scan.

**Figure S8**: Overview of vertical profiles of parameters used as input to the box model utilized in this study which were: 1) from WACCM (temperature, pressure, HCHO); 2) from GEOS-Chem (BrO, $O_3$, $NO_2$, and $Hg^0$); 3) from the TORERO field experiment (total surface area); and 4) derived during this study (BrO and IO).

**Figure S9**: Observed concentrations of selected trace gases during April 2010 at the Pensacola MDN site. Note scale factors for some species given in the legend.

**Figure S10**: Comparison of measured $O_4$ dSCDs and dSCD calculated based on the derived aerosol profiles for the entire case study day (panel a) and a subset of scans (panel b). Panel c contains the diurnal variation in the derived aerosol profiles, and an example profile is found in panel d.

**Figure S11**: Box model results of the rate of mercury oxidation as a function of altitude for two species: 1) ozone (red); and 3) bromine radicals (solid blue: MAX-DOAS; dashed pink: GEOS-Chem) (panel a); the corresponding lifetimes are found in panel b. The black dashed line at 4 km shows where measurement sensitivity starts to drop because of the decreasing amount of BrO (the measured parameter) in the lower layers of the atmosphere. This figure is complementary to Fig. 7, but uses the WACCM, rather than GEOS-Chem, $O_3$ and $NO_2$ vertical profiles as input.

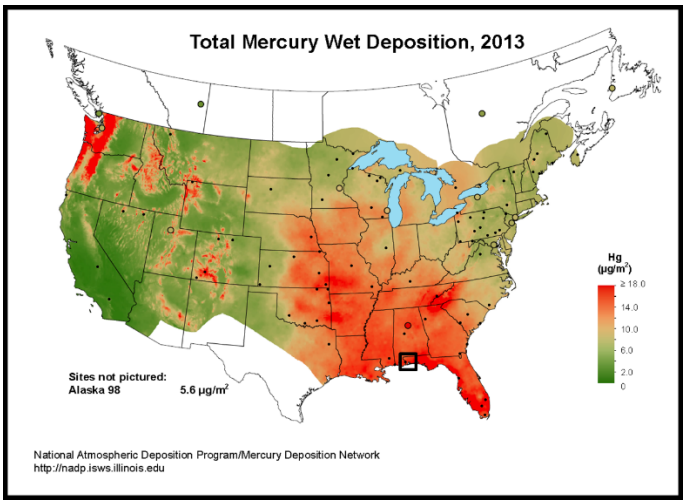


1311

1312 Figure 1

1313

1314 Figure 2

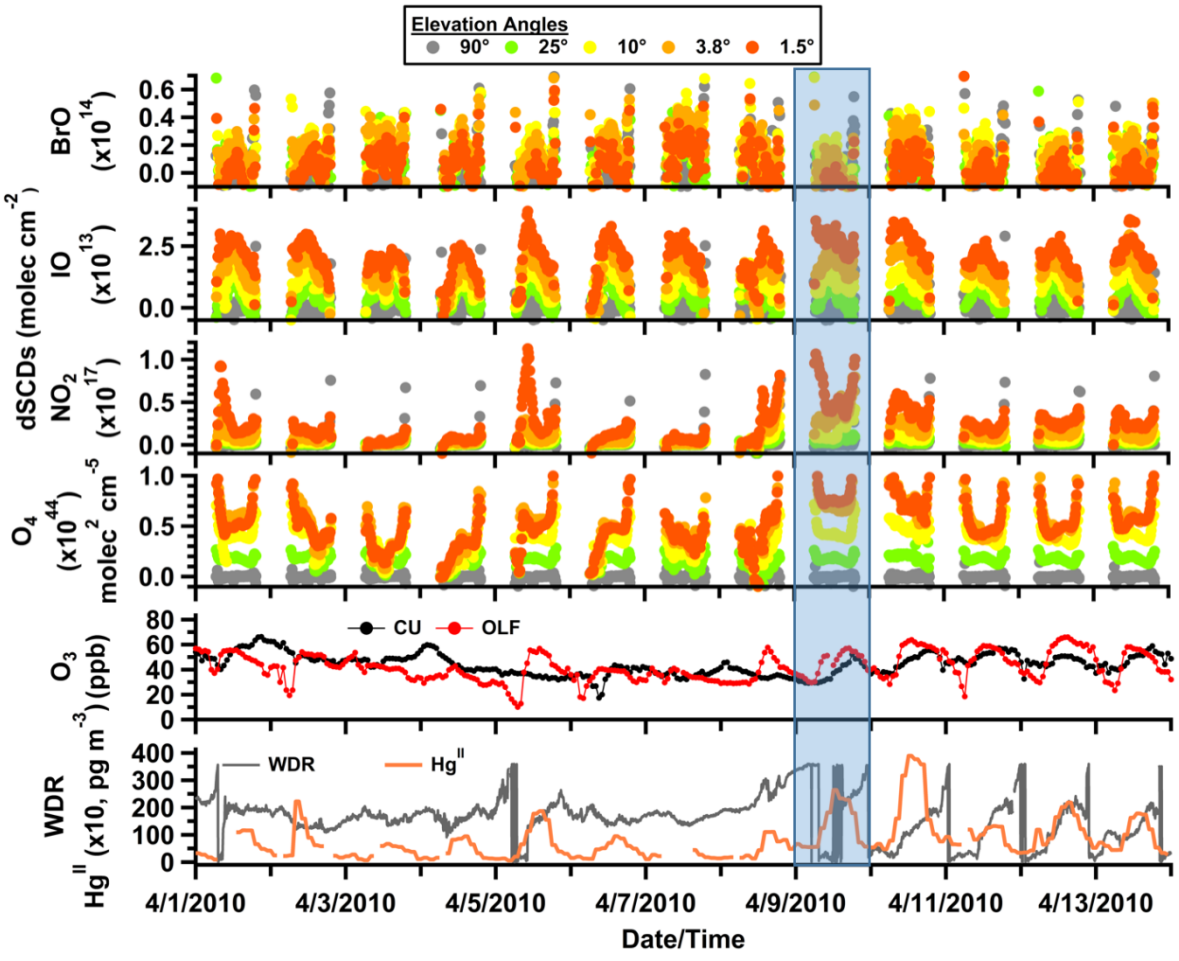


1315

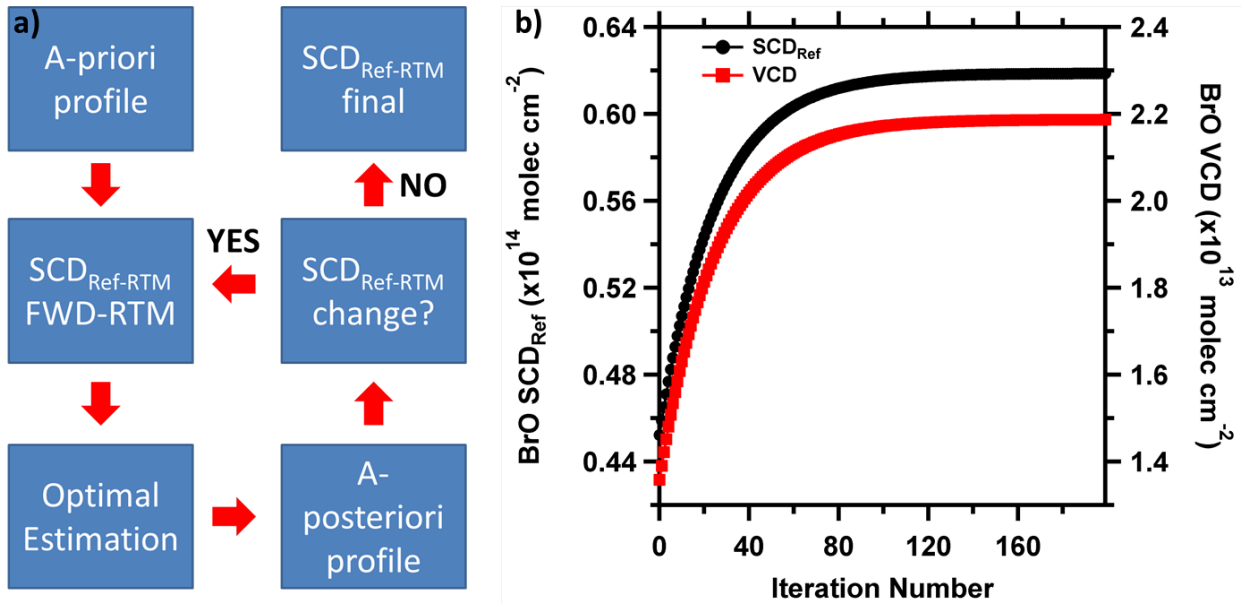
a)
A-priori profile
SCD Ref-RTM FWD-RTM
Optimal Estimation
A-posteriori profile
SCD Ref-RTM change?
SCD Ref-RTM final
YES
NO
b)
SCD Ref
VCD
BrO SCD Ref (x10 14 molec cm -2 )
BrO VCD (x10 13 molec cm -2 )
Iteration Number
0.64
0.60
0.56
0.52
0.48
0.44
2.4
2.2
2.0
1.8
1.6
1.4
0
40
80
120
160

Figure 3

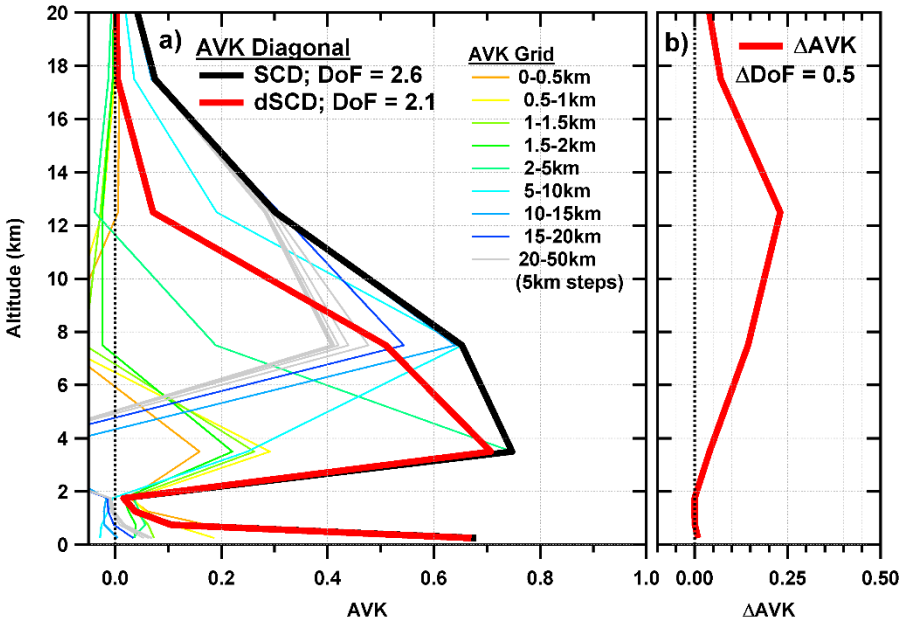
a)
AVK Diagonal
SCD; DoF = 2.6
dSCD; DoF = 2.1
AVK Grid
0-0.5km
0.5-1km
1-1.5km
1.5-2km
2-5km
5-10km
10-15km
15-20km
20-50km
(5km steps)
b)
ΔAVK
ΔDoF = 0.5
Altitude (km)
AVK
ΔAVK

Figure 4

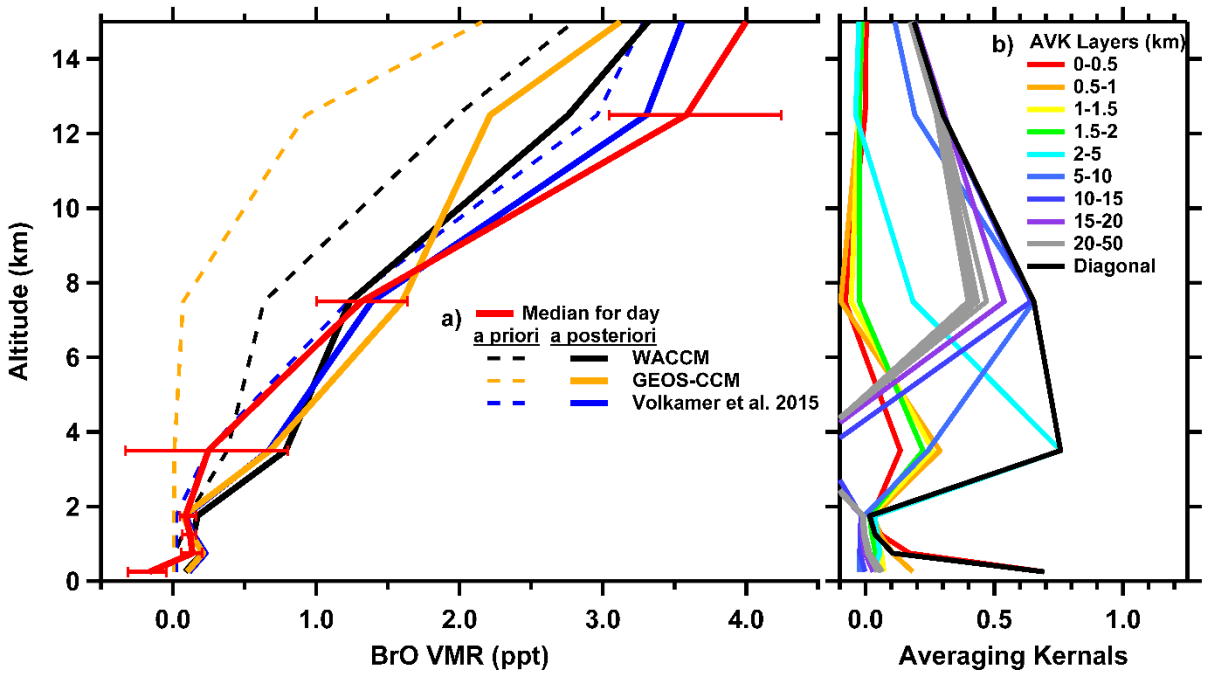
Altitude (km)
BrO VMR (ppt)
a)
Median for day
a priori
a posteriori
WACCM
GEOS-CCM
Volkamer et al. 2015
b)
AVK Layers (km)
0-0.5
0.5-1
1-1.5
1.5-2
2-5
5-10
10-15
15-20
20-50
Diagonal
Averaging Kernals

Figure 5

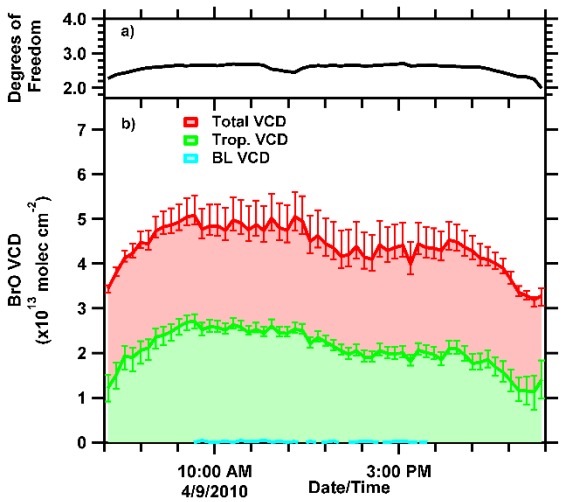


1322

1323 Figure 6

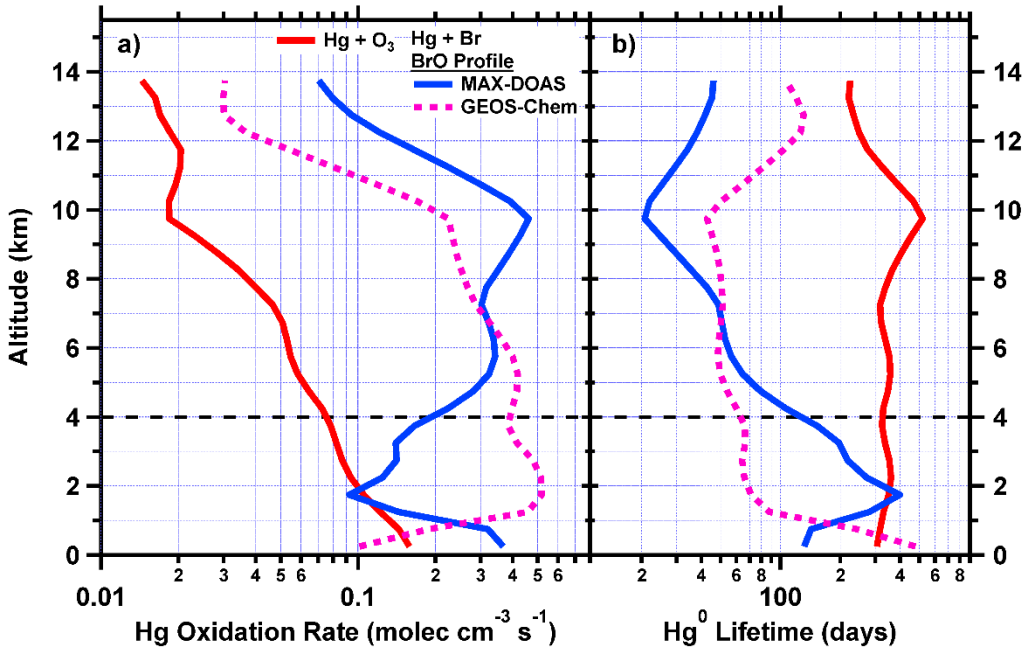


1324

1325 Figure 7

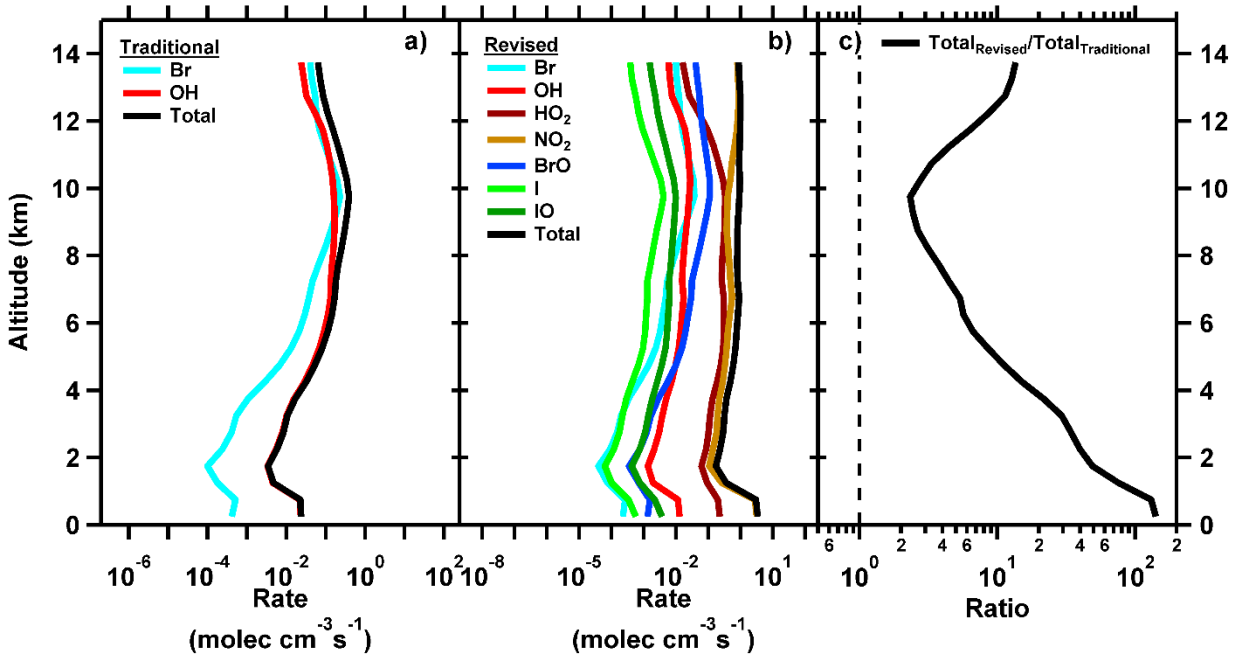
Traditional
Br
OH
Total
a)
Revised
Br
OH
HO2
NO2
BrO
I
IO
Total
b)
c)
Total Revised/Total Traditional
Altitude (km)
Rate
(molec cm-3 s-1)
Rate
(molec cm-3 s-1)
Ratio

Figure 8

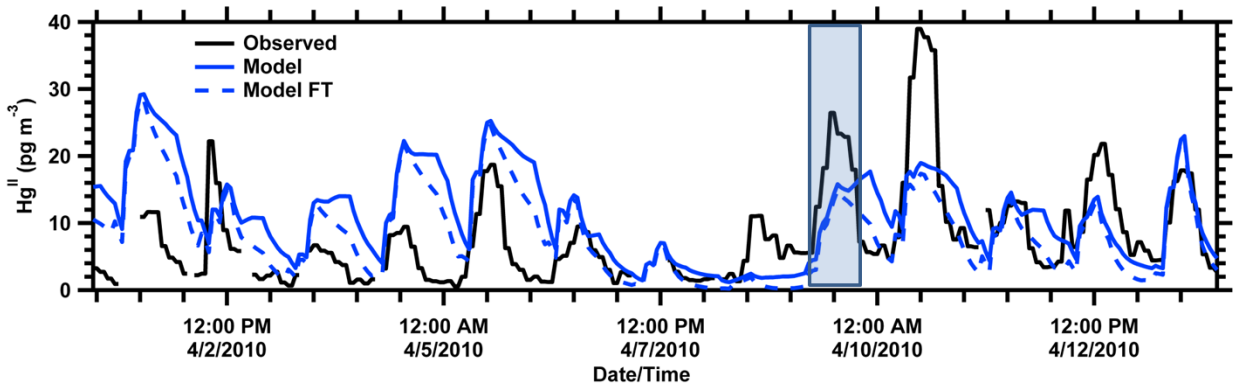
Observed
Model
Model FT
$Hg^{II}$ (pg $m^{-3}$)
40
30
20
10
0
12:00 PM
4/2/2010
12:00 AM
4/5/2010
12:00 PM
4/7/2010
12:00 AM
4/10/2010
12:00 PM
4/12/2010
Date/Time

Figure 9

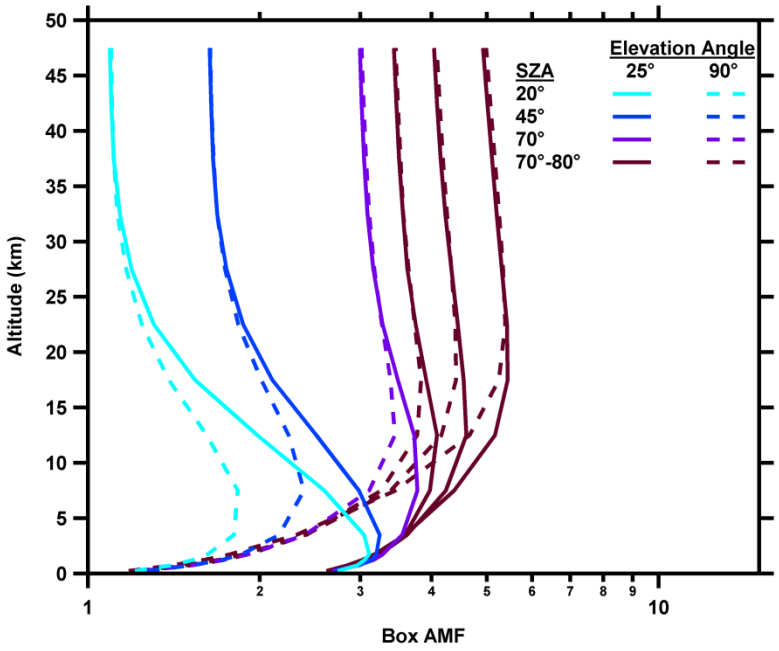


Figure S1

1334

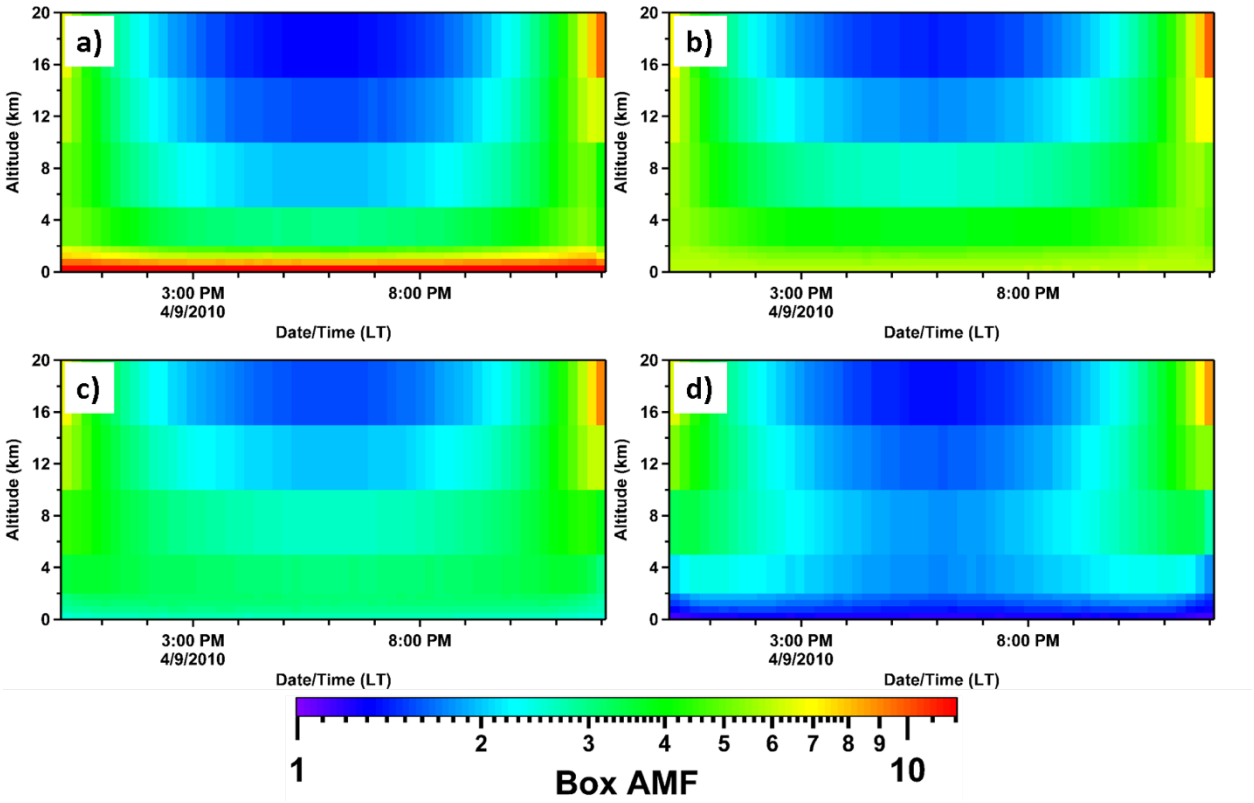


1335

1336 Figure S2

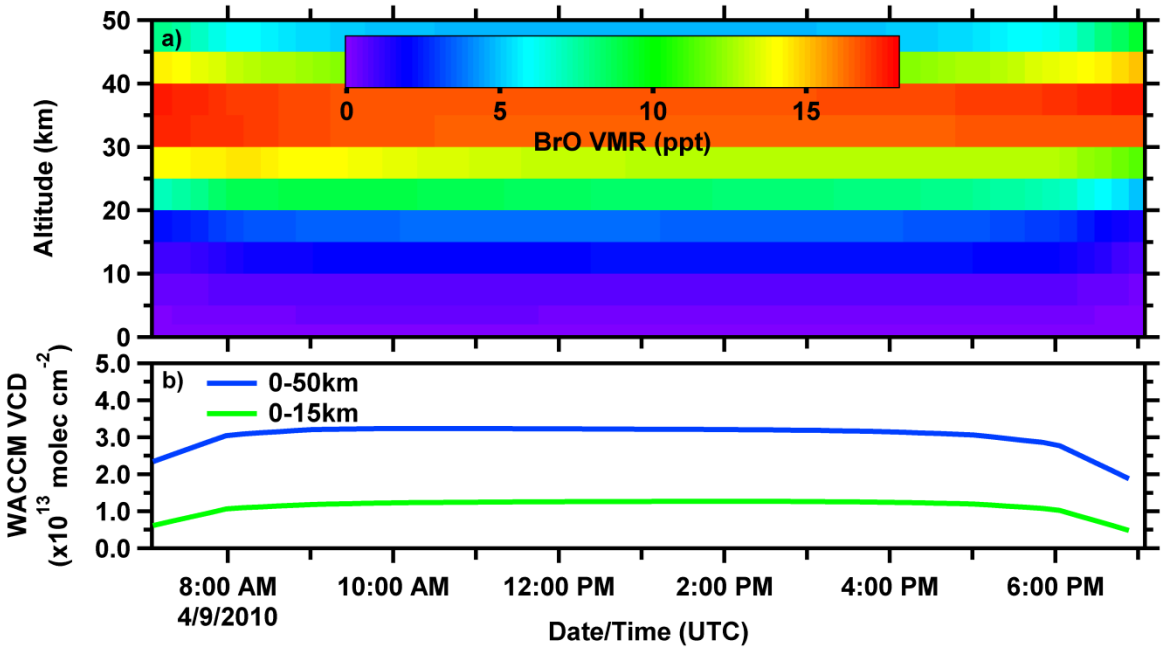


1337

1338 Figure S3

1339

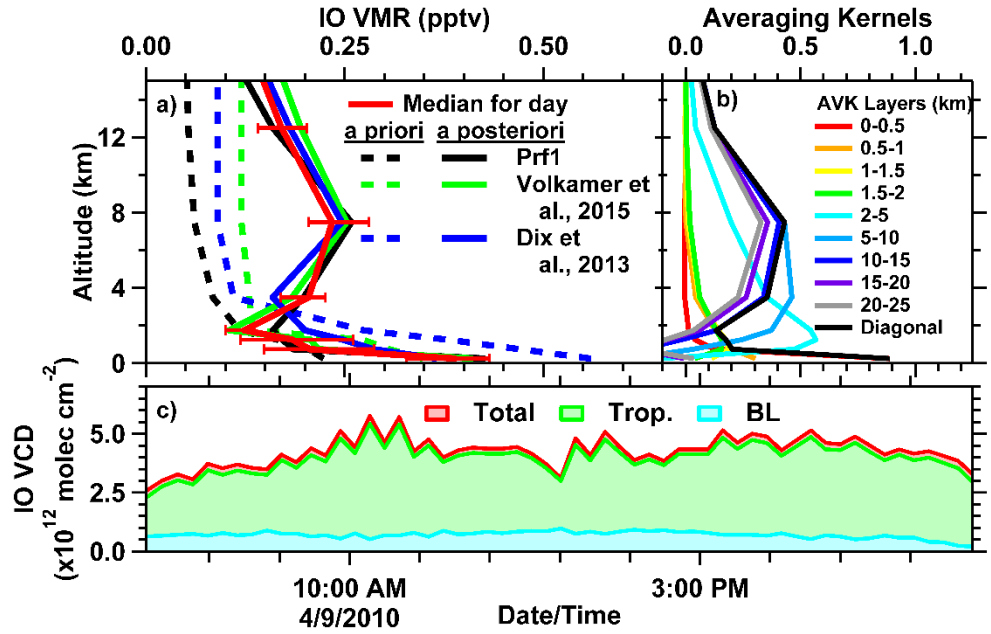


1340

1341 Figure S4

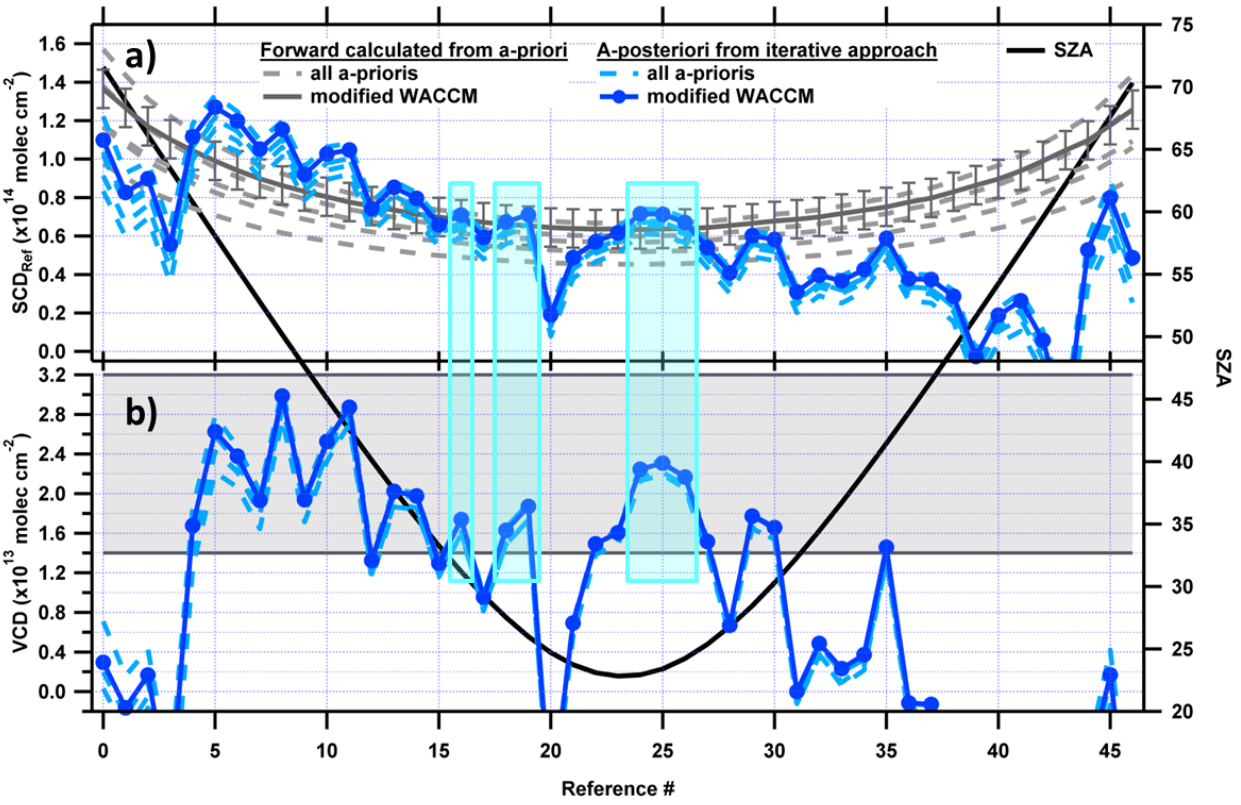


1342

1343 Figure S5

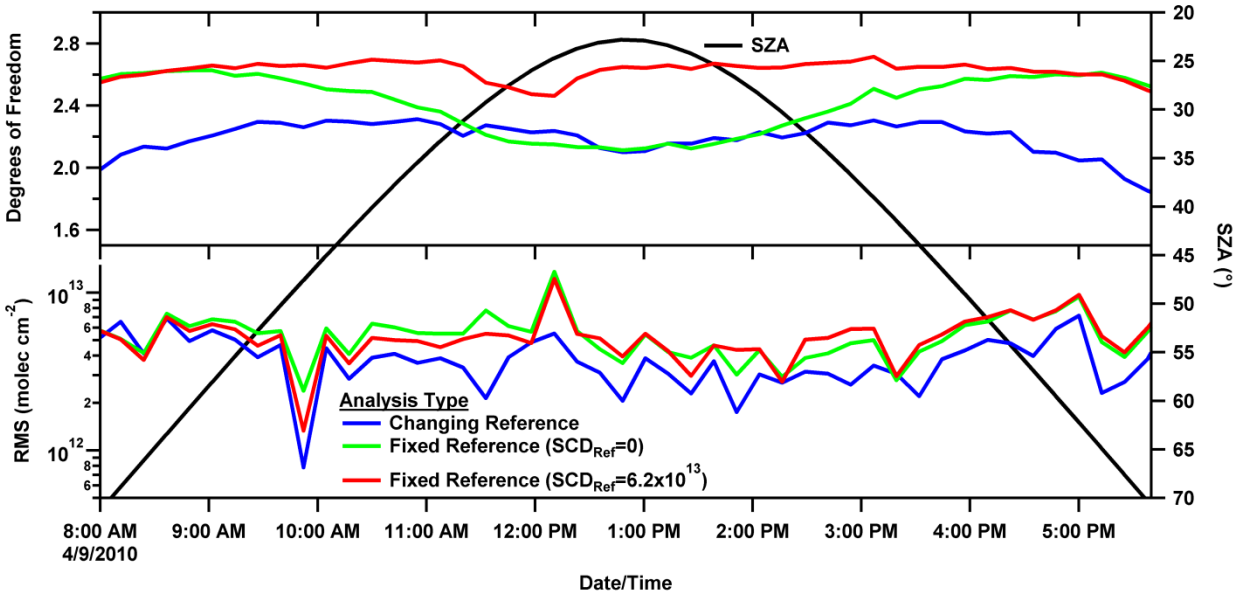


1344

1345 Figure S6

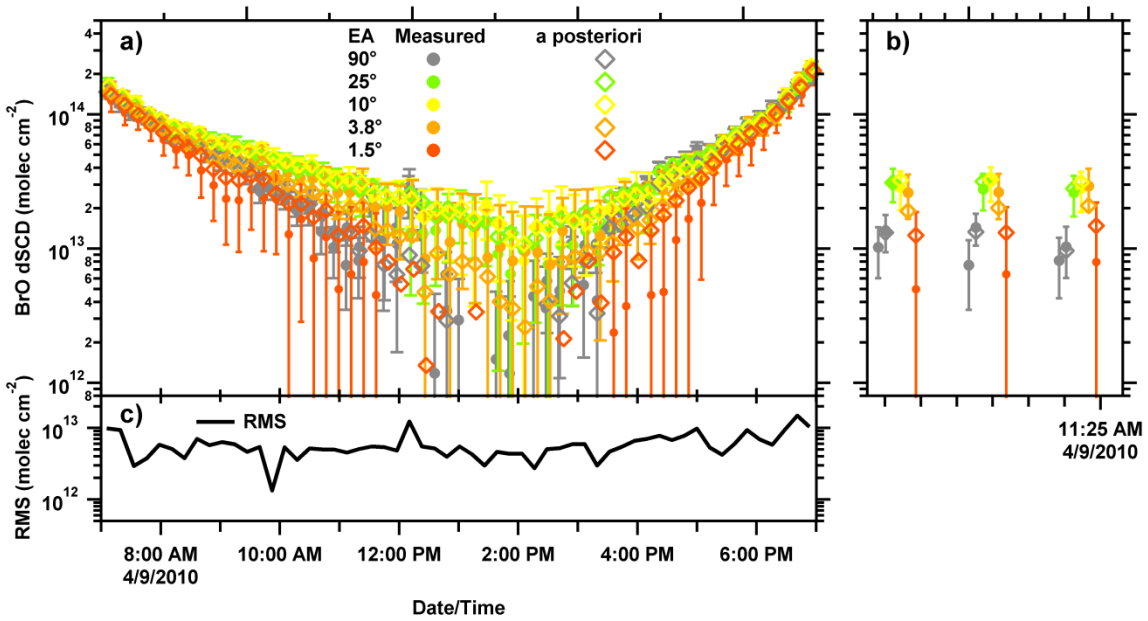


1346

1347 Figure S7

1348

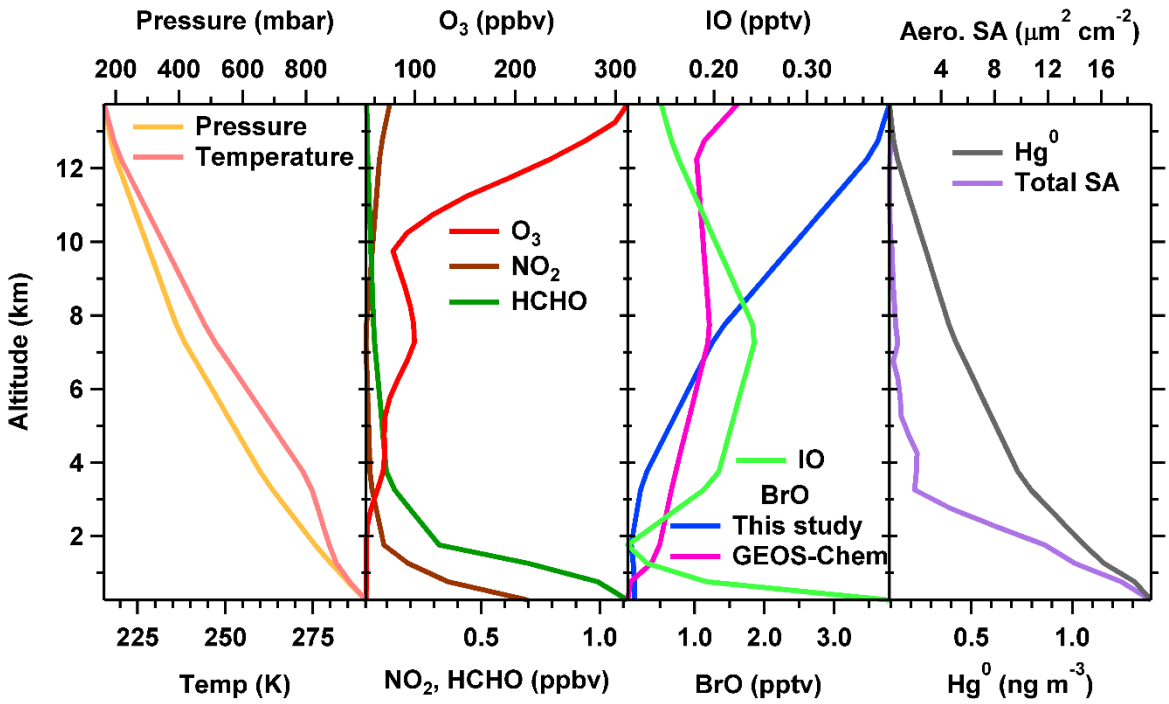


1349

1350 Figure S8

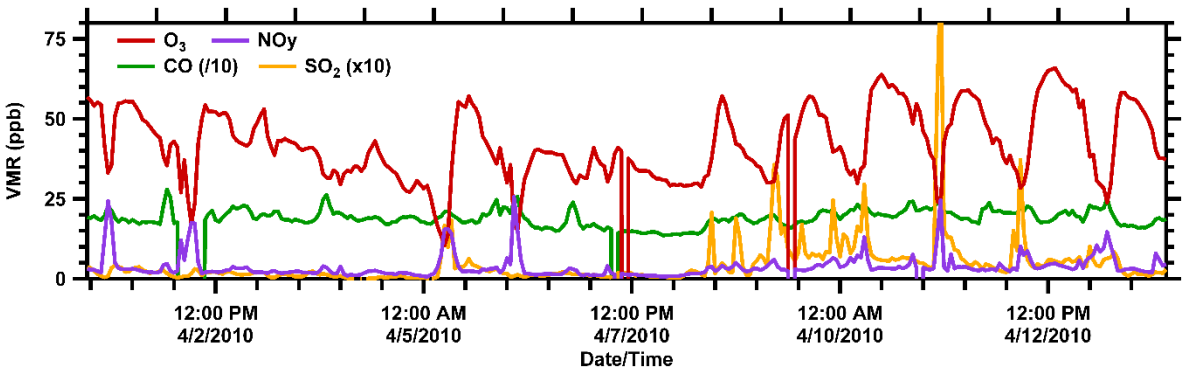


1351

1352 Figure S9

1353

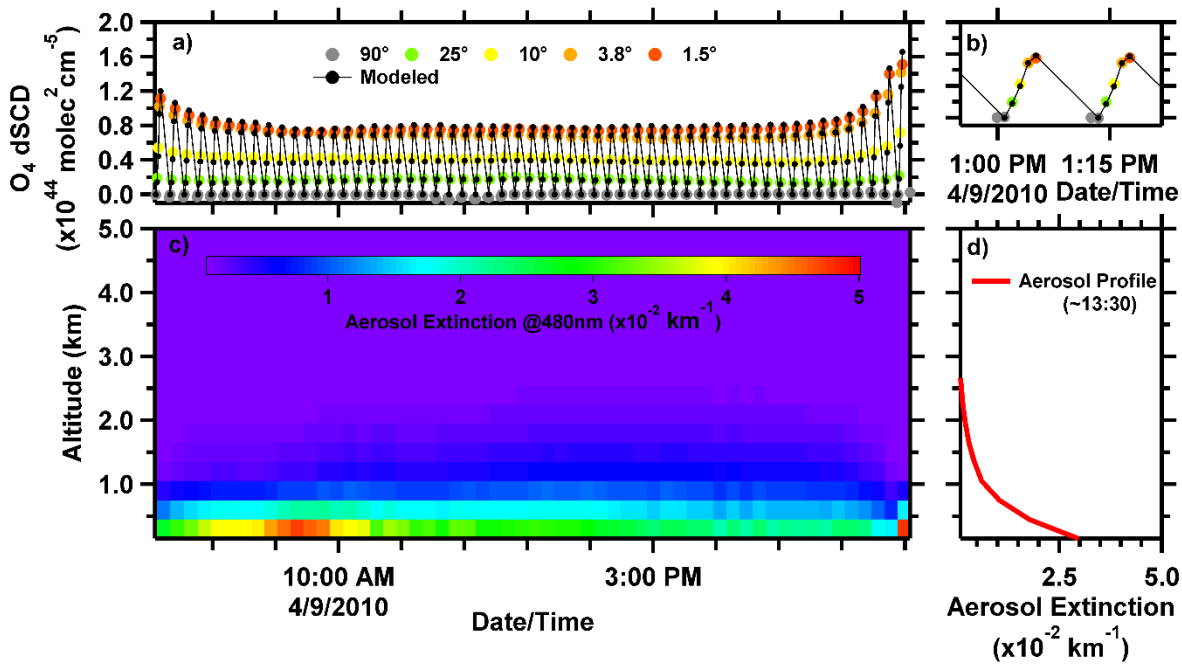


1354
1355 Figure S10

1356

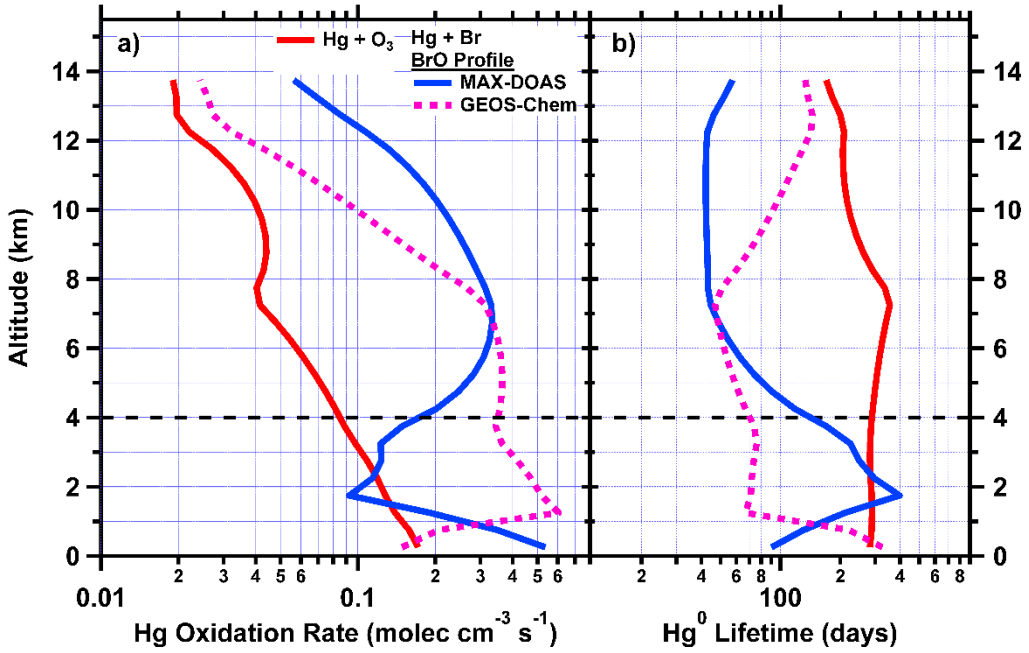


1357

1358 Figure S11

1359